



Robert T. Langland

The five centers of excellence in the Engineering Directorate at Lawrence Livermore National Laboratory (LLNL) are made up of enabling technologies that are essential for these centers to be world class.

However, in addition to the enabling technologies in each center, the Engineering Directorate also has a broad set of supporting technologies that make up the complete capabilities of engineering at LLNL. These allow engineering projects to accomplish specific tasks and make it possible for a program to meet one or more of its objectives or goals.

When appropriate, the Engineering Directorate sponsors work in these supporting technologies. Many efforts are small and do not require significant funding; however, there are some that demand significant resources. The five articles in this section represent some of these more substantial efforts, which are very broad and diverse.

First, we have sponsored a project in multi-scale material modeling that complements a Strategic Initiative funded by LLNL's Laboratory Directed Research and Development Program. This project, "Modeling of Anisotropic Inelastic Behavior," is refining the theory of finite plasticity. It is coordinated with research funded by the National Science Foundation at the University of California at Berkeley. A Ph.D. candidate is using LLNL facilities to develop and carry out very sophisticated testing to map yield surfaces of real materials. The results of this testing will eventually be used in computer codes that have been developed through the leadership of LLNL's Computational Engineering Center.

The second research project, "Modeling Large-Strain, High-Rate Deformation in Metals," has used Hopkinson's bar testing to develop a new model for important materials over a very large range of strain rates, from 10^4 s^{-1} to 10^{-4} s^{-1} . The testing and

material models were done for the aluminum alloy 6061-T6 and the titanium alloy Ti-6Al-4V. These plasticity and failure models apply in tension, compression and shear, and are used in the NIKE and DYNA family of computer codes.

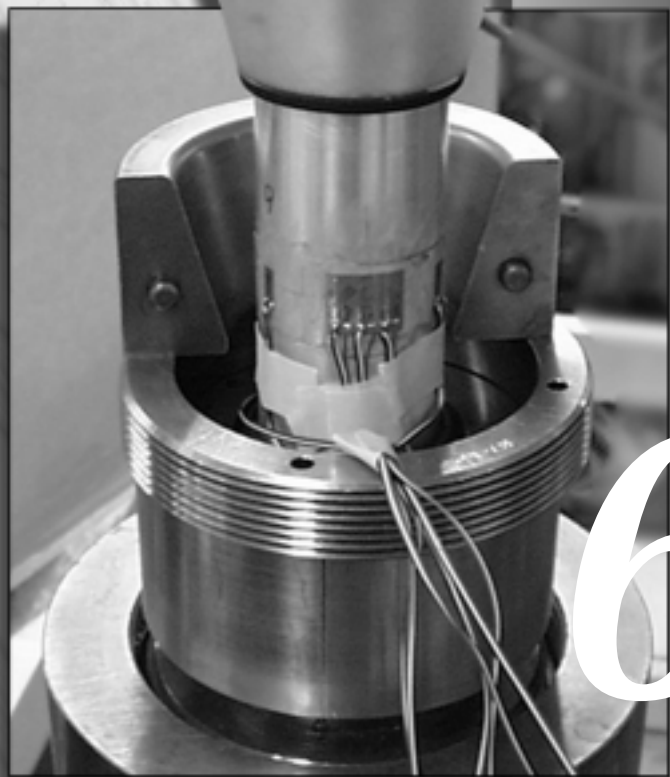
The third project, "Uniform Etching of 85-Cm-Diameter Grating," has developed an ion etching process to build 85-cm-diameter optical grating systems of silicon.

The fourth project, "Distributed Sensor Inertial Measurement Unit," has been funded to refine existing theory to develop, build, test and eventually use an accelerometer-based inertial measurement unit (IMU). This project uses six very sensitive accelerometers with special electronic signal conditioning. These accelerometers are arranged in a critical configuration that permits the definition of the full six degrees of freedom demanded by the application. This approach represents a departure from the use of laser-based rate gyro IMUs, which could not be used for our application.

The fifth project, "Fiber-Based Phase-Shifting Diffraction Interferometer for Measurement and Calibration of the Lick Adaptive Optics System," is transforming a new spherical wavefront-based phase-shifting interferometer into a practical optical measurement system. This project and the one on etching represent examples of an underlying and broad expertise in the design and fabrication of optical systems.

All the projects are working at extreme limits of space and/or time. We are attempting to design, fabricate and perform in areas that are pushing the technologies beyond their current limits. In our supporting technologies, we are exploring and creating new boundaries to meet LLNL's programmatic needs and goals for the future.

Supporting Technologies



6

6. Supporting Technologies

Overview

Robert T. Langland

Modeling of Anisotropic Inelastic Behavior

Daniel J. Nikkel, Jr., Arthur A. Brown, and James Casey 6-1

Modeling Large-Strain, High-Rate Deformation in Metals

Donald R. Lesuer, Mary M. LeBlanc, and Gregory J. Kay 6-7

Uniform Etching of 85-Cm-Diameter Grating

Steven R. Bryan, Jr. and David L. Sanders 6-17

Distributed Sensor Inertial Measurement Unit

Carlos A. Avalle and John I. Castor 6-23

Fiber-Based Phase-Shifting Diffraction Interferometer for Measurement and Calibration of the Lick Adaptive Optics System

Eugene W. Campbell and Jong R. An 6-27

M Modeling of Anisotropic Inelastic Behavior

Daniel J. Nikkel, Jr.

*New Technologies Engineering Division
Mechanical Engineering*

Arthur A. Brown and James Casey

*University of California
Berkeley, California*

We are working to develop better constitutive equations for polycrystalline metals. An experimental capability, developed at Lawrence Livermore National Laboratory (LLNL), is being used to study the yield behavior of elastic-plastic materials. We are directly determining the multi-dimensional yield surface of the material, both in its initial state and as it evolves during large inelastic deformations. These experiments provide a more complete picture of material behavior than can be obtained from traditional uniaxial tests. Experimental results show that actual material response can differ significantly from that predicted by simple idealized models. The yield surface, and its mathematical representation, is an essential component of the constitutive theory for nonlinear anisotropic elastic-plastic materials, and is the main focus of the present project.

Introduction

The ability of numerical simulations to predict the behavior of systems involving materials undergoing large deformations is contingent upon having a realistic model of the behavior of the materials involved. Such models must be accurate in the full range of possible loading conditions that the materials may be subjected to. Use of overly simplified models in regimes where they are not well suited can seriously compromise the validity of a simulation. Many problems of engineering interest involve metal undergoing large deformation under multiaxial states of stress. The need for reliable models for these applications can hardly be overemphasized. As will be seen, simple models for plasticity commonly used in numerical codes do not accurately predict material behavior under these conditions.

From the macroscopic perspective, polycrystalline metals subjected to loads or deformations initially exhibit elastic (reversible) behavior. The material response is path-independent and there is a one-to-one correspondence between stress and strain. However, if the deformation or loads become sufficiently large, the material begins to exhibit plastic behavior (that is, there is no longer a one-to-one correspondence between stress and strain, the

response is dependent on the loading path taken to reach a given state of deformation, and residual—plastic—deformations remain after external loads are removed). This gives rise to the theoretical idealization of an elastic-plastic material, and in particular, to the notion of a yield function¹ denoted by

$$f(s_{kl}, e_{kl}^p, \kappa, \dots) = g(e_{kl}, e_{kl}^p, \kappa, \dots) \quad (1)$$

This function, a key ingredient of the constitutive theory of elastic-plastic materials, describes the boundary between stresses (or strains) that result in only elastic behavior, and those that result in inelastic deformation (**Fig. 1**). In **Eq. 1**, s_{kl} denotes the components of the stress tensor; e_{kl} denotes the components of the strain tensor; e_{kl}^p denotes the components of the plastic strain tensor; κ is a scalar measure of work hardening; and the ellipses represent other inelastic state variables that may be present, depending on the constitutive theory.

Annealed polycrystalline metals typically exhibit isotropic behavior with respect to a reference configuration; that is, at a given point in the material, the material response of a specimen carried out in any direction is the same. This includes the elastic behavior and the initial yield behavior. However, significant processing of materials, or large plastic

deformations, can result in behavior which is anisotropic, where material response in different directions is quite different. Examining the microstructural processes which give rise to inelastic behavior, isotropic behavior can be seen as being due to the random orientation of grains of material, each of which has particular orientations and properties. As a consequence of some types of processing, or due to large inelastic deformations, the initially random grain orientations can become aligned, resulting in anisotropic behavior.

For fixed values of the inelastic variables, the yield condition described by $f = 0$ (or $g = 0$) can be interpreted geometrically from the point of view of stress space (or strain space), the multi-dimensional space whose axes are the components of stress (or strain), as a surface that bounds the region in which only elastic behavior occurs (the elastic region).

As long as the loading of the material is such that the current state is enclosed by the yield surface, the material responds elastically. But, if the loading path intersects the yield surface and tries to cross it, inelastic behavior occurs and plastic deformation results. The current state never moves outside the yield surface, but instead the surface is carried along with it. Typically the yield surface changes shape as the inelastic deformation increases. In addition to the yield function, the constitutive theory includes evolution equations for the inelastic variables during loading ($g = 0$, $\dot{g} > 0$), such as that for the plastic strain:

$$\dot{e}_{kl}^p = \rho_{kl}(e_{mn}, e_{mn}^p, \kappa, \dots)\dot{g},$$

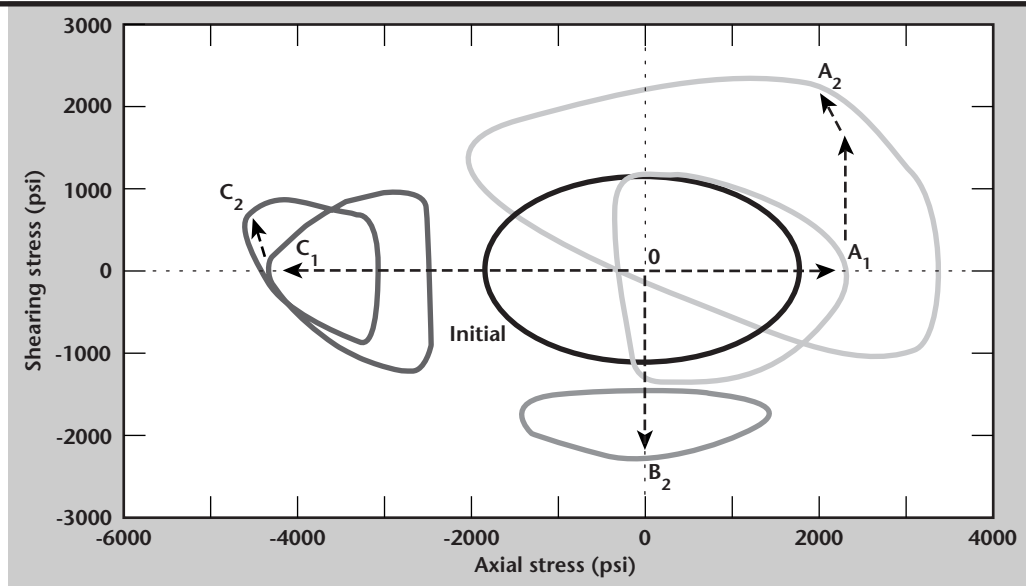
$$\dot{g} \equiv \frac{\partial g}{\partial e_{mn}} \dot{e}_{mn} \quad (2)$$

Here ρ_{kl} is a constitutive response function which is independent of the rates of stress or strain. For a broad class of materials, under a physically reasonable assumption regarding work in closed cycles in strain space, ρ_{kl} can be replaced with the product of scalar function and the normal to the yield surface in stress space, thus requiring the specification of only one additional scalar response function.¹ For special classes of materials, this scalar function is determined from the yield function and hardening and does not require an independent specification.

Most models for plasticity of metals implemented into numerical codes use a yield criterion that corresponds to a fixed shape of the yield surface (for example, elliptical in the case of the Mises yield criterion). What distinguishes different models is how the yield surface is assumed to evolve. For example, it may translate rigidly, or alternatively change its size while maintaining its shape, or follow some combination of these simple hardening laws.

While the initial yield surface of isotropic materials may be represented reasonably well by an ellipse, subsequent to even moderate plastic deformation, the shape of the yield surface in real materials can change significantly (**Fig. 1**). For this reason, simple representations of the yield function will be satisfactory only under very restrictive loading conditions (for example, monotonic or uniaxial), and are totally inadequate for general multiaxial loading conditions where loads can reverse and change direction during the history of loading.

Figure 1. Measured points on yield surfaces in 2-D stress space from three specimens of 1100 aluminum. The subsequent yield surfaces show significant deviation from an idealized ellipse, even though the strains involved are moderately small.



In view of these considerations, and motivated by the fact that the vast majority of experimental data on polycrystalline metals that is available is for uniaxial (and generally monotonic) loading, we developed an experimental capability to map out the yield surface at various fixed states of large inelastic deformation under multiaxial states of loading. By determining the yield surfaces on a single specimen at multiple fixed states, the evolution of the yield surface during plastic deformation can be observed. This data provides the basis for developing improved constitutive equations for polycrystalline metals.

Progress

This project is a combination of a program of novel experiments characterizing inelastic material behavior, together with an effort to develop better material models for implementation into numerical analysis codes. This year, the primary effort has been on the experimental component of the project. Work has also begun examining issues related to numerical implementation of anisotropic plasticity models.

Experiments

The first part of this project involves experiments to directly measure the yield surface. The thin-walled tension-torsion specimen designed for use in a multiaxial MTS hydraulic testing machine is shown in **Fig. 2**. The experimental determination of the yield surface of the material is carried out by loading a specimen under multiaxial conditions and probing until the point of yield is reached, then backing off and probing in a different direction in stress space (and in strain space) until the next yield point is found. This process is repeated until the entire surface is mapped out. The sensitive nature of the measurements being made requires careful attention to the issues of specimen design and preparation, experimental methodology, and interpretation of the data.

The general description of the experiments and the difficulty in carrying out these measurements has been discussed previously.² The present discussion will focus on refinements that have been made during FY-98.

The surface that we are trying to map represents the yield surface at an arbitrary fixed inelastic state. Ideally, all points on a given yield surface should be determined without inducing any further plastic deformation to the specimen. In practice, however, a point on the yield surface can only be determined by reaching, and slightly exceeding, the yield point. Each time

the yield point is exceeded in this way, the inelastic state, and the yield surface itself, are slightly changed.

For our purposes, it is important to minimize this distortion of the yield surface. To characterize a given surface, a number of points on it must be located (probably a minimum of 10) while changing the inelastic state (hence, the surface itself) as little as possible. The way in which yield is defined experimentally can significantly affect the yield surface which is determined.

A number of alternative definitions have been investigated, and the effects of different definitions on the resulting measured yield surfaces have been studied. The procedure which has been developed can detect yield without producing a plastic strain much greater than 5×10^{-6} . We refined the experimental procedure to reduce a number of sources of error and have demonstrated that the methodology for determining yield surfaces is repeatable.

The importance of rate effects has also been investigated. Even in materials which are not considered highly rate-sensitive, due to the

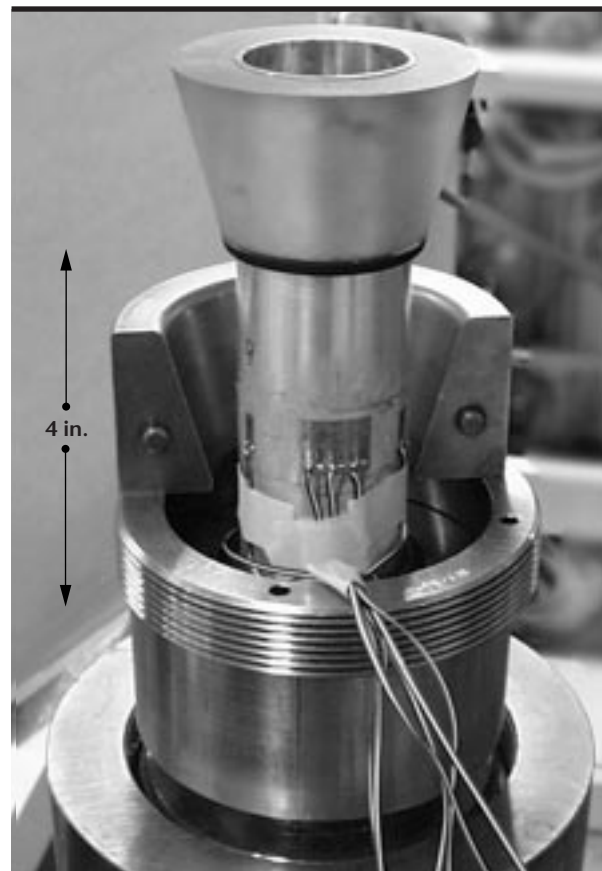


Figure 2. Thin-walled biaxial test specimen that can be subjected to tension, compression and torsion, used to measure points on the yield surface of the material. The yield surface at several different states can be measured from one specimen.

desired accuracy in measuring the yield surface, it was found necessary to run the tests very slowly, increasing the time required to complete each measurement.

In addition to generating data from the measurement of yield surfaces, we are also seeking to address the fundamental question of the proper definition of plastic strain in the context of large inelastic deformations.^{3,4} We have successfully measured yield surfaces that have moved so that they no longer enclose the origin in stress space (for example, paths O-B₂ and O-C₁-C₂ in **Fig. 1**).

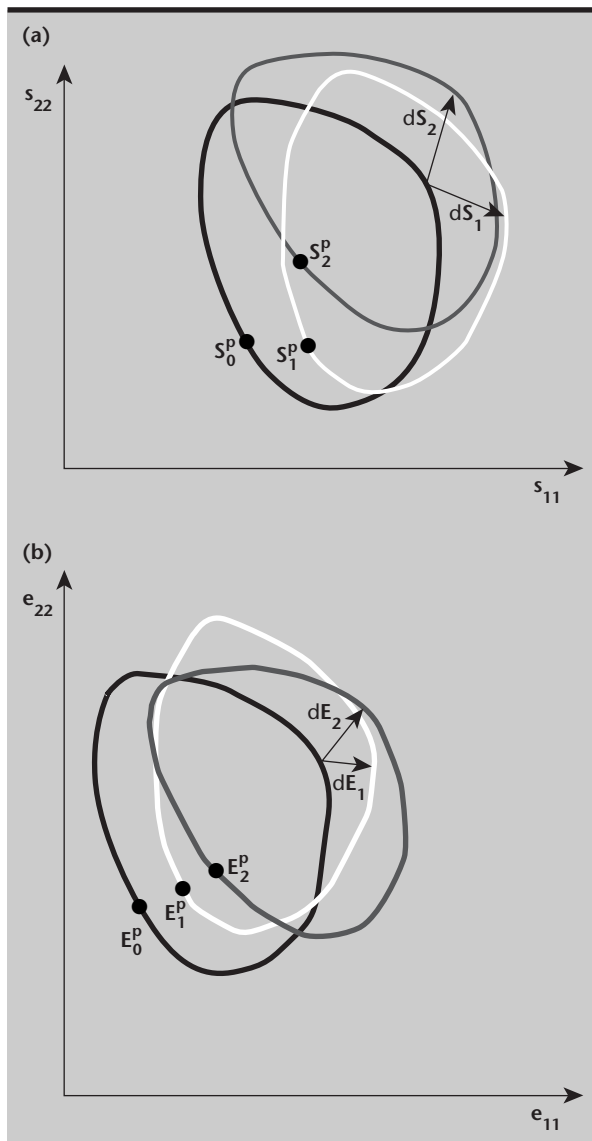


Figure 3. Schematic of the experimental method for verifying the prescription for plastic strain viewed in (a) stress space, and (b) strain space. From a fixed arbitrary state (darkest yield surface), the change due to plastic increments on paths of two differing directions is measured. Colinearity of the points E_0^p , E_1^p , and E_2^p in strain space verifies the proposed prescription.

In this situation, the material cannot be unloaded to zero stress without causing new plastic deformations. The traditional way of defining plastic strain is to identify it with the residual strain remaining when the load is removed. This definition arose intuitively from consideration of uniaxial tests with small deformation, but it is clearly inadequate in the situation of more general states of loading where the yield surface no longer encloses the origin in stress space.

Plastic strain is not among the set of kinematic variables that come from classical continuum mechanics. Since it is a primitive variable in the constitutive theory, one must be able to unambiguously identify it for the theory to be meaningfully predictive and not simply a sophisticated curve-fit.

In view of **Eq. 2**, while the magnitude of the plastic strain increment depends on the strain increment, its direction does not. The direction is the same as the direction of the tensor, ρ_{kl} , which depends only on the current state and not on rates of stress or strain. This fact will be used to verify the validity of the prescription for identifying plastic strain.^{3,4}

Two or more specimens will be loaded to an arbitrary inelastic state where the yield surface in stress space does not enclose the origin. The specimens will then be given small plastic load increments starting from the same point on the yield surface, but having different directions in strain space. This is shown schematically in **Fig. 3**, in both (2-D) stress and strain space. The point closest to the origin on a given yield surface in stress space is designated as S^p , and the corresponding state in strain space is identified as the plastic strain tensor, E^p .

The darkest yield surface in **Fig. 3** represents a known arbitrary state. The two lighter surfaces represent two subsequent yield surfaces obtained from the first by loading in two different directions. If the prescription^{3,4} is valid, the resulting plastic strain increments for the two cases should have the same direction, although they may vary in magnitude. Thus, colinearity of the points E_0^p , E_1^p , and E_2^p in **Fig. 3b** would verify the prescription.

Modeling

We have begun efforts to model the anisotropic material behavior exhibited in the experiments, and to explore issues related to numerical implementation of anisotropic models. The Mises yield condition, which is a quadratic polynomial in the

deviatoric stress components, is known to agree well with experimental data on annealed (isotropic) polycrystalline metals, and it also has a physically appealing interpretation in terms of distortion energy.

For anisotropic materials, the most general quadratic yield function representing a smooth initial yield surface that reduces to the Mises yield function in the special case of isotropic materials is of the form⁵

$$f = B_{klmn} s_{kl} s_{mn} - \kappa^2, \quad (3)$$

where the coefficient tensor, B_{klmn} , has the obvious symmetries, and hence has 21 independent components. If, as is commonly done, the further assumption is made that the yield behavior is independent of the mean stress (pressure), then the stress in **Eq. 3** can be replaced by the deviatoric stress, and the coefficient tensor can be replaced by a reduced tensor which has 15 independent coefficients.

The yield function (**Eq. 3**) contains as a special case the anisotropic yield condition of Hill which is available in the DYNA code and is sometimes used in sheet metal forming analyses. Even though **Eq. 3** is much more general than the Mises yield function, it still does not adequately represent the kinds of material behavior exhibited in **Fig. 1**. It does, however, provide a reasonable basis to begin exploring some of the issues associated with implementing anisotropic plasticity models into numerical codes.

To evaluate some of these issues, the yield function (**Eq. 3**) was implemented into the parallel version of the ALE3D code. **Figure 4** shows the results of the simulation of a thick-walled anisotropic sphere (initial radius = 10, initial wall thickness = 2) subjected to a uniform external pressure load. With isotropic material properties, the sphere symmetrically compresses as one would expect. By modifying the properties in one direction, the very non-symmetric response in **Fig. 4** is predicted, indicating the significant effect that material anisotropy can have on overall structural response.

For Mises-type yield functions, an efficient numerical procedure for integrating the evolution equations has long been used. This consists of an elastic trial step followed by a radial-return corrector step. This simple and efficient procedure does not work in general for anisotropic yield functions, and one of the challenges ahead will be in developing robust, numerically efficient procedures for integrating the anisotropic evolution equations. In the context of the nonlinear strain-space formulation of the theory of elastic-plastic materials,

Papadopoulos and Lu⁶ have developed a method for integrating the evolution equations, which for the special case of transversely isotropic materials reduces to computing three separate radial-return steps for three orthogonal parts of the solution.

In addition to this effort to develop a phenomenological continuum model using experimental data, an effort is also underway to develop a homogenization methodology to predict effective macroscopic behavior based on explicit consideration of microstructural features, such as the statistical distribution of grain orientations. To this end, a material model for single crystal plasticity has been implemented into NIKE3D. This model also has the capability to account for polycrystal aggregates at each integration point using Taylor averaging. This model can be used in numerical experiments to predict effective yield surfaces for explicit microstructural configurations.

Future Work

We now have confidence in our ability to measure yield surfaces as accurately as necessary for our purposes. Continued work will involve generating specific data sets to guide the development of better constitutive equations for nonlinear plasticity. The anisotropic yield function (**Eq. 3**), while a useful starting point for evaluating some of the basic numerical issues, is not sufficiently general to represent the behavior we are seeing in the data. We will be focusing on developing a better theoretical model to represent the yield surface and its evolution.

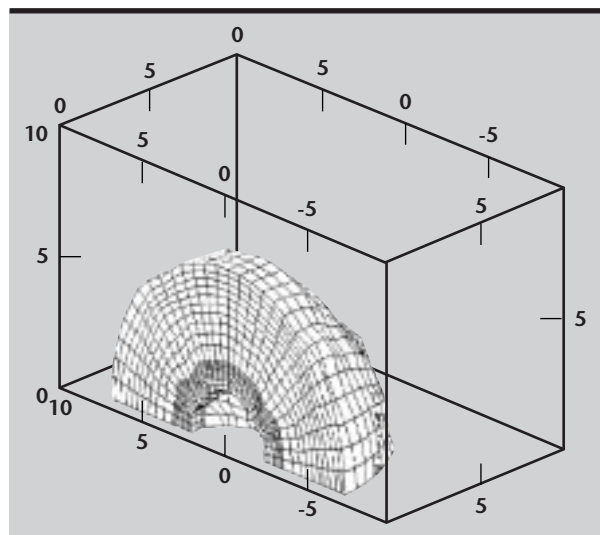



Figure 4. Numerical simulation of a sphere of homogeneous but anisotropic material, subjected to a uniform external pressure. For isotropic material properties, the sphere would compact symmetrically.

We also plan to examine materials of particular relevance to LLNL programs, relevance such as tantalum, which is a target material for the Multiscale Material Modeling effort. We also plan to complete the experiments discussed above to address the question of the correct identification of the plastic strain tensor in the context of general finite deformations.

Acknowledgment

Contributions to this project from Prof. J. Casey result from work supported by a grant from the Solid Mechanics Program of the National Science Foundation. Part of support for A. Brown's work, and material used during the development of the experimental procedure, were also provided through this grant.

References

1. Naghdi, P. M. (1990), "A Critical Review of the State of Finite Plasticity," *J. Appl. Math. and Phys. (ZAMP)*, **41**, pp. 315-394.
2. Nikkel, D. J., A. A. Brown, and J. Casey (1998), "Evolution of Anisotropic Yield Behavior," *Engineering Research, Development and Technology*, Lawrence Livermore National Laboratory, Livermore, California (UCRL-53868-97), pp. 5-1-5-5.
3. Casey, J., and P. M. Naghdi (1992), "A Prescription for the Identification of Finite Plastic Strain," *Int. J. Engng. Sci.*, **30**, pp. 1257-78.
4. Casey, J., and P. M. Naghdi (1992), "On the Identification of Plastic Strain at Finite Deformation," in *Defects and Anelasticity in the Characterization of Crystalline Solids*, L. M. Brock, ed., ASME AMD Vol. **148**, pp. 11-33.
5. Green, A. E., and P. M. Naghdi (1965), "A General Theory of an Elastic-Plastic Continuum," *Arch. Rat. Mech. and Anal.*, **18**, pp. 251-281.
6. Papadopoulos, P. and J. Lu (1998), "A General Framework for the Numerical Solution of Problems in Finite Elasto-Plasticity," *Comp. Meth. in Appl. Mech. and Engng.*, **159**, pp. 1-18. 

M Modeling Large-Strain High-Rate Deformation in Metals

Donald R. Lesuer and Mary M. LeBlanc

*Manufacturing and Materials Engineering Division
Mechanical Engineering*

Gregory J. Kay

*New Technologies Engineering Division
Mechanical Engineering*

The large-strain deformation responses of aluminum alloy 6061-T6 and titanium alloy Ti-6Al-4V have been evaluated over a range in strain rates from 10^{-4} s^{-1} to $>10^4 \text{ s}^{-1}$. The results have been used to critically evaluate the strength and damage components of the Johnson-Cook (JC) material model. Two new models that address the short-comings of the JC model were then developed and evaluated. One model is derived from the rate equations that represent deformation mechanisms active during moderate- and high-rate loading; the other model accounts for the influence of void formation on yield and flow behavior of a ductile metal (the Gurson model). The characteristics and predictive capabilities of these models are reviewed.

Introduction

Many modeling problems of interest to Lawrence Livermore National Laboratory (LLNL) involve accurate representation of the high-rate deformation response of materials. Examples include the modeling of material processing operations as well as the in-service performance of materials. Typical material processing operations, in which high-rate deformation is observed, include material cutting, numerous forming operations (such as rolling and forging) and material polishing. Typical in-service performance problems include the ballistic penetration and perforation of armor materials, the performance of munitions, and explosive fragmentation.

Many of these problems are difficult to model accurately. Much of this difficulty arises from the large strains and adiabatic heat produced, which, in turn, causes increases in temperature with resulting changes in material microstructure, material properties, and deformation mechanisms. Large changes in strain rate are also produced.

In addition, deformation can produce instabilities in the form of adiabatic shear bands. Voids can also be produced that can influence flow behavior and serve as a precursor to fracture. Thus, accurate material models are necessary for understanding deformation behavior (and strength) as well as failure response.

Objectives

Material models that can adequately represent the deformation response during high-rate loading must account for large strains (and the resulting strain hardening or softening), as well as large changes in strain rate and temperature. Several models have been developed that can represent, to varying degrees, the high-rate deformation response of materials. Examples include models by Johnson and Cook (JC),¹⁻³ Zerilli and Armstrong (ZA),⁴⁻⁶ and Follansbee and Kocks (mechanical threshold stress model)⁷.

Two of these models (JC and ZA) have been introduced into LLNL's DYNA codes.

Of these two models, the JC model is much more widely used. The JC model was developed during the 1980s to study impact, ballistic penetration, and explosive detonation problems. The model has proven to be very popular and has been used extensively by a number of national laboratories, military laboratories, and private industry to study high-rate, large-strain problems. The reasons for the popularity of this model include the simple form of the constitutive equations and the availability of constants used in the equations for a number of materials. The JC material model also has a cumulative damage law that can be used to assess failure.

In this report, we take a critical look at the JC model and its ability to represent the large-strain deformation behavior of two important structural materials: an α - β titanium alloy (Ti-6Al-4V) and a moderate strength aluminum alloy (6061-T6). The model has been evaluated over a range of strain rates from 10^{-4} s^{-1} to $>10^4 \text{ s}^{-1}$. The damage law was also evaluated for its ability to predict failure in these materials. Two new models were then developed and evaluated that address some of the shortcomings observed with the JC model. One of the models is derived from the rate equations that represent deformation mechanisms active during moderate- and high-rate loading; the other model accounts for the influence of void formation on yield and flow behavior of a ductile metal (the Gurson model⁸). The characteristics and predictive capabilities of these models are reviewed.

Progress

Materials, Experiments and Results

The materials used in this study were obtained from commercial sources. The 6061 alloy was received as a hot, cross-rolled plate in the T6 temper. The Ti-6Al-4V alloy was obtained according to the AMS 4911 specification, which produced an equiaxed α and transformed β microstructure.

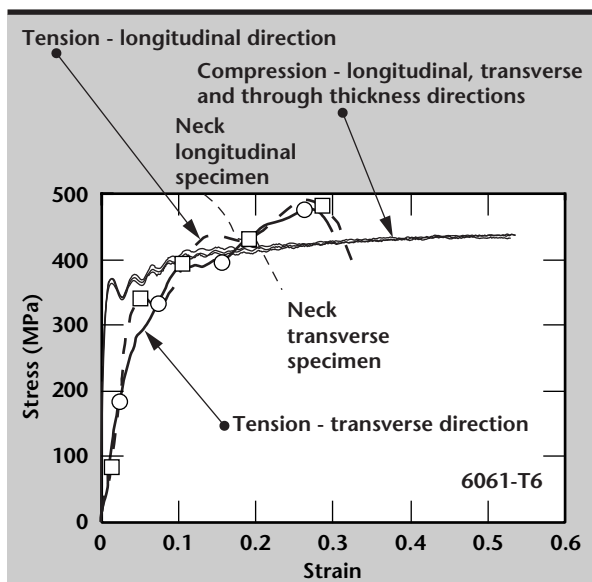


Figure 1. Stress-strain data for aluminum alloy 6061-T6 obtained in tension and compression with the split Hopkinson pressure bar apparatus. The experiments in tension were conducted in two different orientations and at a strain rate of 8000 s^{-1} . The experiments in compression were conducted in three different orientations and at a strain rate of 4000 s^{-1} .

High-rate testing was done in both compression and tension using the split Hopkinson pressure bar technique, and data was obtained at strain rates of 10^3 s^{-1} to 10^4 s^{-1} . In the compression tests, the strain histories for the incident and transmitted waves in the elastic pressure bars were measured and analyzed to determine the nominal stress/strain/strain-rate response of the sample. In the tension tests, the strain history in the elastic pressure bars was used to obtain the stress-time response of the sample. The strain and strain-rate behavior of the sample was obtained from high-speed photographic images derived from a framing camera.

All stress-strain data is provided as “true stress” and “true strain.” The stress-strain data for 6061-T6 aluminum obtained in tension and compression is shown in **Fig. 1**. The experiments in tension were conducted at a strain rate of 8000 s^{-1} , and samples were tested with the tensile axis parallel to the longitudinal and transverse orientations in the plate. The experiments in compression were conducted at a strain rate of 4000 s^{-1} , and samples were tested with the compression axis parallel to the longitudinal, transverse, and through-thickness orientations in the plate.

Data for “elastic” loading of the sample can not be obtained in these tests due to wave propagation effects. The stress-strain data shown in **Fig. 1** can be considered valid once the samples have yielded plastically, which is accompanied by stress and strain rate uniformity in the sample. The data for the different orientations of testing show that in both tension and compression, the stress-strain response is highly isotropic. This is especially true in compression, in which the curves for the three orientations fall virtually on top of one another. The compression samples deformed to the limits of the experiment without failure, while the tension samples failed after a strain of 0.26.

Johnson-Cook Material Model

The formulation for the JC model is empirically based and represents the flow stress with an equation of the form

$$\sigma = \left[A + B\epsilon^n \right] \left[1 + C \ln \dot{\epsilon}^* \right] \left[1 - T^{*m} \right] \quad (1)$$

where σ is the effective stress, ϵ is the effective plastic strain, $\dot{\epsilon}^*$ is the normalized effective plastic strain rate (typically normalized to a strain rate of 1.0 s^{-1}), T^* is the homologous temperature, n is the work hardening exponent and A , B , C , and m are constants.

The values of A , B , C , n , and m are determined from an empirical fit of flow stress data (as a function

Table 1. Johnson-Cook constants for Ti-6Al-4V and 6061-T6.

	A (MPa)	B (MPa)	n	C	m	D ₁	D ₂	D ₃	D ₄	D ₅
6061-T6	324	114	0.42	0.002	1.34	-0.77	1.45	-0.47	0.0	1.60
Ti-6Al-4V	862	331	0.34	0.012	0.8	-0.09	0.25	-0.5	0.014	3.87

of strain, strain rate and temperature) to **Eq. 1**. For high-rate deformation problems, we can assume that an arbitrary percentage of the plastic work done during deformation produces heat in the deforming material. For many materials, 100% of the plastic work becomes heat in the material. Thus the temperature used in **Eq. 1** can be derived from the increase in temperature according to the following expression

$$\Delta T = \frac{\alpha B}{\rho c(n+1)} \epsilon^{n+1}, \quad (2)$$

where ΔT is the temperature increase, α is the percentage of plastic work transformed to heat, c is the heat capacity and ρ is the density.

Fracture in the JC material model is derived from the following cumulative damage law:

$$D = \sum \frac{\Delta \epsilon}{\epsilon_f}, \quad (3)$$

where

$$\epsilon_f = \left[D_1 + D_2 \exp(D_3 \sigma^*) \right] \left[1 + D_4 \ln \dot{\epsilon}^* \right] \left[1 + D_5 T^* \right], \quad (4)$$

$\Delta \epsilon$ is the increment of effective plastic strain during an increment in loading and σ^* is the mean stress normalized by the effective stress. The parameters D_1 , D_2 , D_3 , D_4 , and D_5 are constants. Failure is assumed to occur when $D = 1$. The current failure strain (ϵ_f) is thus a function of mean stress, strain rate, and temperature. The constants for the JC model used in the evaluations in the next section are given in **Table 1**.

Model Evaluation. The adiabatic stress-strain behavior for the 6061-T6 alloy predicted by the JC material model is shown in **Fig. 2** for loading in tension, compression, and shear. The cumulative damage predicted by the failure model is also shown in the figure, and the failure strains for the three stress states are indicated on the stress-strain curve. The three stress curves show different damage curves because of the influence of the mean stress term on ϵ_f in **Eq. 4**.

The stress-strain response predicted by the material model is compared against the experimental data in both tension and compression in **Fig. 3**. The yield

strength predicted by the JC model correlates very well with the experimental results. However, the experimental stress-strain curves work harden at a higher rate. This is not a fundamental short-coming of the model, since higher work hardening rates are possible with larger values of B and n in **Eq. 1**. The failure strain in tension as predicted by the JC material model ($\epsilon_f = 0.52$) is significantly higher than that obtained experimentally ($\epsilon_f = 0.26$). This is a significant difference and the physical origins of this discrepancy need to be understood. However, detailed studies of failure models are outside the scope of this paper.

The stress-strain rate response for the 6061-T6 alloy is compared against the predictions of the JC model in **Fig. 4**. Data was obtained from the work of Nicholas⁹ as well as from this study. Here significant deviations between model predictions and experimental results are evident. The experimental data shows a dramatic increase in strength above a strain rate of 10^3 s^{-1} . This increase in strength has been observed in a number of metals¹⁰ and is generally recognized as resulting from a change in deformation mechanism.

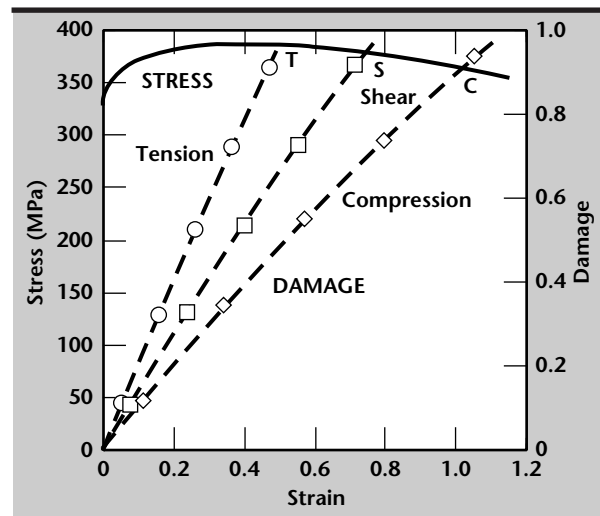


Figure 2. Adiabatic stress-strain behavior for aluminum alloy 6061-T6 at a strain rate of 6000 s^{-1} predicted by the JC material model. Results are presented for loading in tension, compression, and shear. The cumulative damage predicted by the material model is also shown. The failure point along the stress-strain curve is shown for tension, shear, and compression.

At lower strain rates, the deformation rate is controlled by the cutting or by-passing of discrete obstacles by dislocations. At higher rates, the deformation rate is controlled by phonon or electron drag on moving dislocations. These two mechanisms are represented by different deformation rate equations, which results in the dramatic change in behavior from low strain rates to high strain rates. Such dramatic changes are outside the scope of the JC model. In the next section we present a model that accounts for these mechanism changes.

The predictions of the JC model for the Ti-6Al-4V alloy are shown in **Fig. 5** and compared against experimental data in **Figs. 6** and **7**, obtained from the work of Wulf¹¹, Meyer¹² and Follansbee and Gray¹³. The same capabilities and limitations of the material model that were observed for the 6061-T6

alloy were noted for the Ti-6Al-4V alloy. The model can adequately represent work-hardening behavior in both materials. The most serious limitation is its ability to predict variations of flow stress with strain rate, as shown in **Fig. 7**. The failure model predicted the correct ductility in tension for the Ti-6Al-4V alloy ($\epsilon_f = 0.15$) but, in compression, the model predicted a significantly higher ductility than that observed experimentally.

Mechanism-Based Material Model

Rate Equations. We now derive a rate equation representing deformation that can be controlled by two sequential processes: 1) the cutting (or by-passing) of obstacles by dislocations, or 2) the drag on moving dislocations by phonons or electrons. The

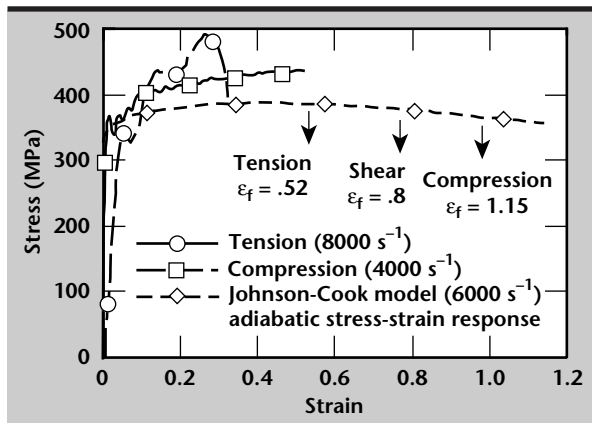


Figure 3. Comparison between the stress-strain behavior predicted by the JC material model and experimental data for aluminum alloy 6061-T6.

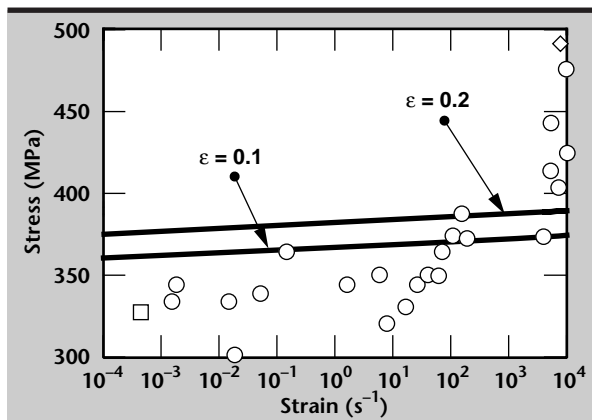


Figure 4. Comparison between the stress-strain rate behavior predicted by the JC material model and experimental data for aluminum alloy 6061-T6. Experimental data is derived from a compilation of LLNL results and data from Reference 9.

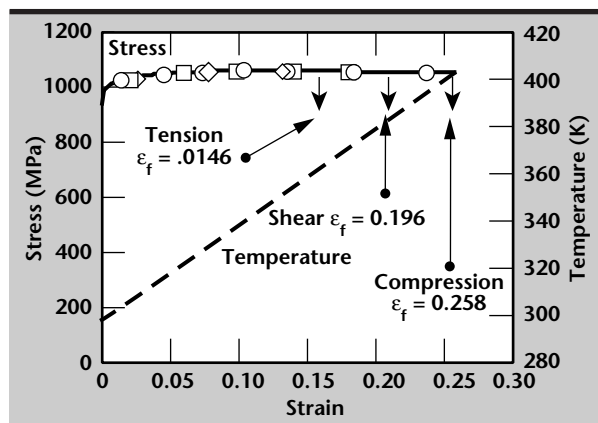


Figure 5. Adiabatic stress-strain behavior for titanium alloy Ti-6Al-4V at a strain rate of 5000 s⁻¹, as predicted by the JC material model. Results are presented for loading in tension, compression, and shear. The adiabatic temperature rise is also shown. The failure point along the stress-strain curve is shown for the three stress states.

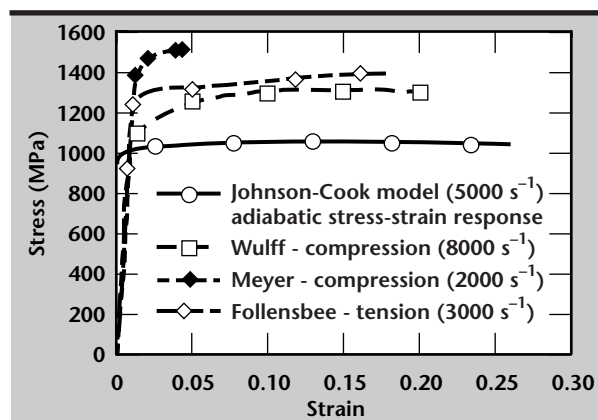


Figure 6. Comparison between the stress-strain behavior predicted by the JC material model and experimental data for titanium alloy Ti-6Al-4V (obtained from References 11 to 13).

problem is illustrated schematically in **Fig. 8**, which shows dislocations in contact with discrete obstacles that have an average spacing, d . After Frost and Ashby¹⁴, the average velocity, v , for a dislocation moving through these obstacles is

$$v = d / (t_1 + t_2), \quad (5)$$

where t_1 is the time required to cut or by-pass the obstacle, and t_2 is the time spent moving to the next obstacle. Different rate equations represent the deformation kinetics associated with discrete obstacles and drag. Let $\dot{\epsilon}_1$ represent the strain rate when deformation is controlled by the cutting or by-passing of discrete obstacles, and $\dot{\epsilon}_2$ represent the strain rate when deformation is controlled by drag on moving dislocations. Since

$$\dot{\epsilon} = \rho b v, \quad (6)$$

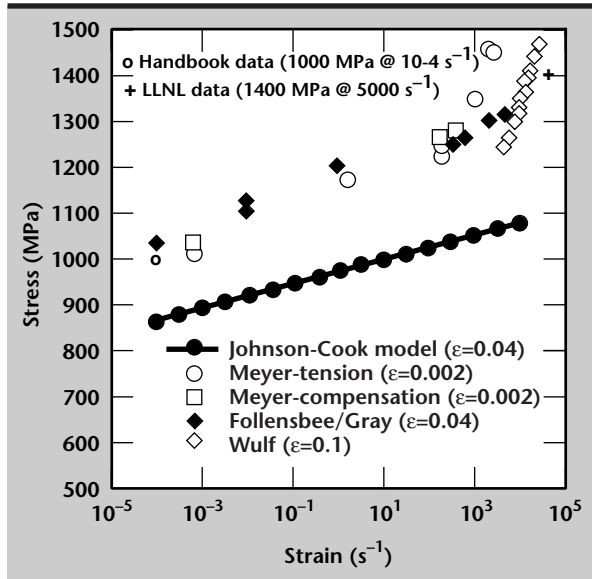


Figure 7. Comparison between the stress-strain rate behavior predicted by the JC material model and experimental data for aluminum alloy 6061-T6.

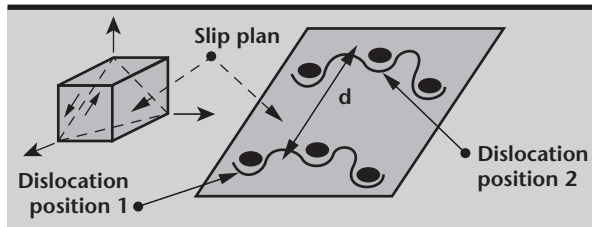


Figure 8. Dislocations on a slip plane in contact with discrete obstacles. The shear stress on the slip plane is σ , and the average spacing between obstacles is d . At high strain rates, the dislocation velocity (and therefore strain rate) is determined by the rate at which the discrete obstacles are by-passed, or the rate at which the dislocation moves from one discrete obstacle to the next.

where $\dot{\epsilon}$ is the strain rate, b is the Burger's vector and ρ is the mobile dislocation density,

$$\dot{\epsilon}_{\text{eff}} = \frac{d}{\frac{d}{\dot{\epsilon}_1} + \frac{d}{\dot{\epsilon}_2}}, \quad (7)$$

where $\dot{\epsilon}_{\text{eff}}$ is the effective strain rate on the slip plane shown in **Fig. 8**. Thus

$$\dot{\epsilon}_{\text{eff}} = \frac{\dot{\epsilon}_1 \dot{\epsilon}_2}{\dot{\epsilon}_1 + \dot{\epsilon}_2}. \quad (8)$$

The rate equation for discrete obstacle controlled plasticity¹⁵ can be taken as

$$\dot{\epsilon}_1 = \dot{\epsilon}_0 \exp \left[-\frac{Q}{kT} \left(1 - \frac{\sigma}{\tau} \right) \right], \quad (9)$$

where $\dot{\epsilon}_0$ is a constant, Q is an activation energy, k is Boltzmann's constant, σ is the stress and τ is the strength of the obstacle. At constant temperature, the equation can be taken as

$$\dot{\epsilon}_1 = A \exp(B\sigma), \quad (10)$$

where A and B are constants. The rate equation for phonon- or electron-drag-controlled plasticity can be taken as

$$\dot{\epsilon}_2 = C\sigma^D, \quad (11)$$

where C and D are constants. Several theoretical treatments have shown that D approaches 1^{16,17}. We will use the general form of the rate equation shown in **Eq. 11**. **Equations 8, 10, and 11** can now be used to calculate the strain rate resulting from the sequential mechanism of discrete-obstacle plasticity and drag-controlled plasticity.

Model Evaluation. The model, as represented by **Eqs. 8, 10, and 11**, was evaluated against the stress-strain rate data for the 6061-T6 and Ti-6Al-4V alloys shown in **Figs. 4 and 7**, respectively. The constants for obstacle-controlled plasticity (A and B) were evaluated in the strain-rate range where this mechanism is dominant. Similarly, the constants for drag-controlled plasticity (C and D) were evaluated in the strain-rate range where this mechanism is dominant.

Figure 9 shows a comparison of the stress-strain rate response predicted by the mechanism-based material model and experimental data for the 6061-T6 alloy.

Similarly, **Fig. 10** shows a comparison of the stress-strain rate response predicted by the mechanism-based material model and experimental

data for the Ti-6Al-4V alloy. The figures also show the regions of the stress-strain curves that are dominated by discrete-obstacle plasticity and by drag-controlled plasticity. For both alloys, the agreement between the model predictions and experimental data is excellent.

Gurson Void Growth Model

Observations have been made that ductile fracture in metals is related to the nucleation and growth of voids. Conventional plasticity models, for example, von Mises, are based on the assumption of plastic incompressibility and can not predict the growth of voids during yielding. Studies have indicated^{18–20} that void growth during tensile loading is related to the hydrostatic component of stress, and that this porosity increase directly affects material yielding.

In these observations it was assumed that the material surrounding a void was incompressible. Gurson⁸ proposed a pressure-sensitive macroscopic yield surface that relates void growth to the evolution of microscopic (pointwise physical quantities of the matrix material) and macroscopic quantities to account for the behavior of void-containing solids. Here, macroscopic refers to the average values of physical quantities, which represent the material aggregate behavior. As defined by Gurson, the yield surface for a ductile material is:

$$\Phi = \left(\frac{q}{\sigma_0} \right)^2 + 2q_1 f \cosh \left(\frac{3p}{2\sigma_0} \right) - \left(1 + q_2 f^2 \right) = 0, \quad (12)$$

where σ_0 is the tensile flow stress of the microscopic matrix material, q and p are the equivalent

stress and hydrostatic stresses of the macroscopic material, and f is the current void volume fraction which is a function of the initial porosity, the void growth, and nucleation during yielding. The material parameters q_1, q_2 are defined by Gurson.

The Gurson model was added to NIKE2D by B. Engelmann. For the current study, a version of the NIKE2D Gurson model was modified to correctly account for the evolution of plastic strain in the micro (matrix) material and to account for strain rate sensitivity. The model was added to DYNA3D.

The response of a notched bar under uniaxial tensile loading was simulated to demonstrate the DYNA3D application of the Gurson model. Substantial hydrostatic tension is created in the notched regions of the bar for this type of loading. This hydrostatic stress accelerates void growth and leads to the eventual coalescence of voids and ductile failure of the bar. Failure was assumed to correspond to the loss of load-carrying capability in this displacement-controlled simulation.

The bar was assumed to have the following material properties: $E = 20.7$ GPa, $\nu = 0.3$, yield stress = 690 MPa, with a linear hardening modulus of 1,540 MPa. The initial void fraction was assumed to be equal to 0.050.

The initial and deformed shapes of the tensile specimen are shown in **Fig. 11**, which also depicts the regions of predicted high void growth. The effect of rate-dependence is shown in **Fig. 12**, where an increased loading rate resulted in an increased normalized axial load (actual axial load/initial yield strength), with softening similar to the rate-independent Gurson model results.

Also shown in **Fig. 12** is the conventional plasticity solution, which does not exhibit the

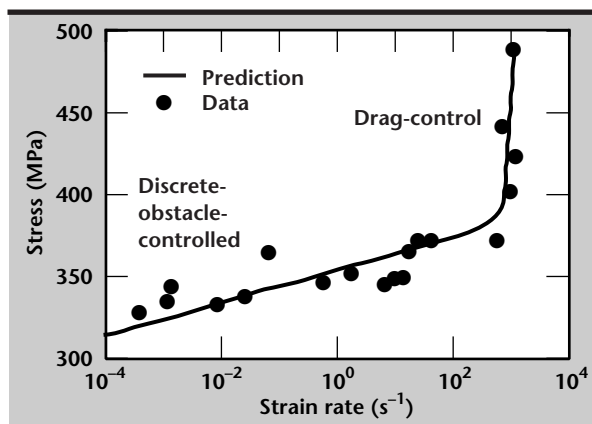


Figure 9. Comparison between the stress-strain rate behavior predicted by the mechanism-based material model and experimental data for aluminum alloy 6061-T6. Regions of the stress-strain rate curve that are dominated by discrete-obstacle plasticity and drag-controlled plasticity are shown.

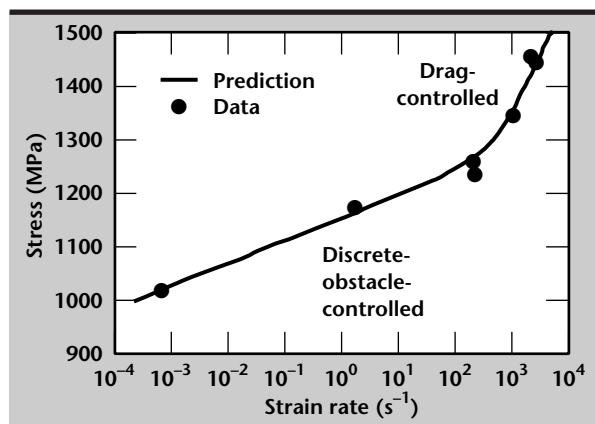


Figure 10. Comparison between the stress-strain rate behavior predicted by the mechanism-based material model and experimental data for titanium alloy Ti-6Al-4V. Regions of the stress-strain rate curve that are dominated by discrete-obstacle plasticity and drag-controlled plasticity are shown.

pronounced softening predicted by the Gurson model. The conventional plasticity yield surface is also shown to be larger, with a higher strain-to-failure, than the porous material, a result confirmed by experimental results.

For this simulation, the final void fraction was 0.70. A calculation was also performed to check the sensitivity of the solution to mesh size. The mesh in this calculation was twice the density of the initial simulation. The results of this calculation

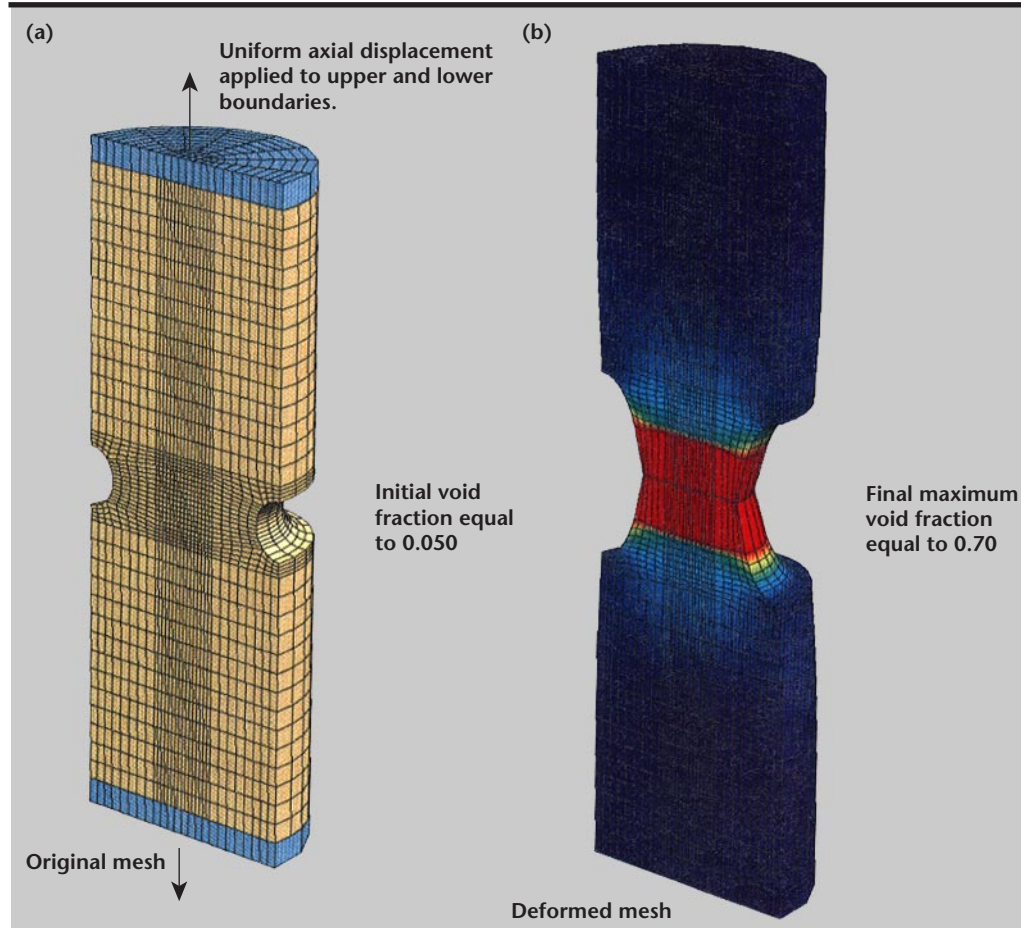


Figure 11. Notched tensile specimen void growth, as predicted by the Gurson model.

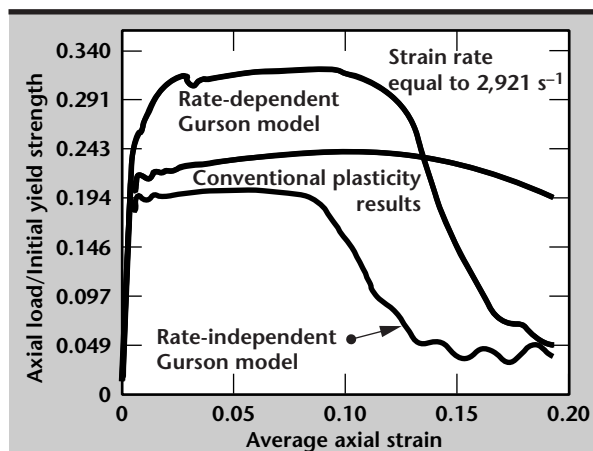


Figure 12. Gurson model rate effects for a notched bar under displacement-controlled axial loading.

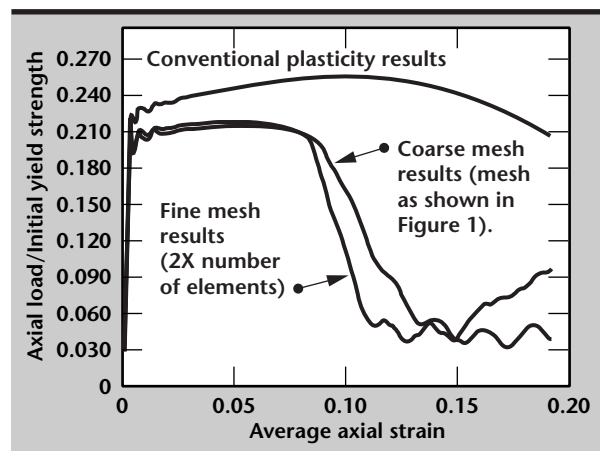


Figure 13. Gurson model mesh sensitivity for a notched bar under displacement-controlled axial loading.

tion, shown in **Fig. 13**, indicate that there is some small mesh sensitivity of the solution, in the post-failure phase, for the rate-independent Gurson solution.


Summary

The primary conclusions and observations relative to the three models studied are as follows:

1. JC model. For the alloys studied, the JC model can accurately represent the yield and work-hardening behavior of the materials. The JC model predicts higher failure strains than those observed experimentally. The most serious short-coming of the JC model is its inability to accurately represent the variation of flow stress with strain rate.
2. Deformation mechanism model. This model accounts for two sequential deformation mechanisms that are active at moderate- and high-deformation rates. The mechanisms are discrete-obstacle plasticity and drag-controlled plasticity. The model has been developed and evaluated against stress-strain rate data for the 6061-T6 alloy and the Ti-6Al-4V alloy. Agreement between experimental results and model predictions is excellent.
3. Gurson void growth model. The Gurson void growth model has been introduced into the DYNA3D code. The model was modified to account for the evolution of plastic strain and strain rate sensitivity. The model was used in the DYNA3D code to simulate the response of a notched bar during tensile loading.

References

1. Johnson, G. R., and W. H. Cook (1985), "Fracture Characteristics of Three Metals Subjected to Various Strains, Strain Rates, Temperatures and Pressures," *Engineering Fracture Mechanics*, **21**, No. 1, pp. 31–48.
2. Johnson, G. R., and W. H. Cook (1983), "A Constitutive Model and Data for Metals Subjected to Large Strains, High Rates and High Temperatures," *Proceedings of the Seventh International Symposium on Ballistics*, The Hague, The Netherlands, pp. 541–547.
3. Johnson, G. R., and T. J. Holmquist (1988), "Evaluation of Cylinder-Impact Test Data for Constitutive Model Constants," *Journal of Applied Physics*, **64**, No. 8, pp. 3901–3910.
4. Zerilli, F. J., and R. W. Armstrong (1987), "Dislocation-Mechanics-Based Constitutive Relations for Material Dynamics Calculations," *Journal of Applied Physics*, **61**, No. 5, pp. 1816–1825.
5. Zerilli, F. J., and R. W. Armstrong (1990), "Description of Tantalum Deformation Behavior by Dislocation Mechanics Based Constitutive Equations," *Journal of Applied Physics*, **68**, No. 4, pp. 1580–1591.
6. Zerilli, F. J., and R. W. Armstrong (1992), "The Effect of Dislocation Drag on the Stress-Strain Behavior of FCC Metals," *Acta Metallurgica et Materialia*, **40**, No. 8, pp. 1803–1808.
7. Follansbee, P. S., and U. F. Kocks (1988), "A Constitutive Description of the Deformation of Copper Based on the Use of the Mechanical Threshold Stress as an Internal State Variable," *Acta Metallurgica*, **36**, pp. 81–93.
8. Gurson, A. J. (1977), "Continuum Theory of Ductile Rupture by Void Nucleation and Growth, Part I - Yield Criteria and Flow Rules for Porous Ductile Media," *Journal of Engineering Materials Technology*, **99**, pp. 2–15.
9. Nicholas, T. (1981), "Tensile Testing of Material at High Rates of Strain," *Experimental Mechanics*, May, pp. 177–185.
10. Follansbee, P. S. (1986), "High-Strain-Rate Deformation of FCC Metals and Alloys," in *Metallurgical Applications of Shock-Wave and High-Strain-Rate Phenomena*, L. E. Murr, K. P. Staudhammer, and M. A. Meyers, eds. New York: Marcel Dekker, Inc., pp. 451–479.
11. Wulf, G. L. (1979), "High Strain Rate Compression of Titanium and Some Titanium Alloys," *International Journal of Mechanical Sciences*, **21**, pp. 713–718.
12. Meyer, L. W. (1984), "Strength and Ductility of a Titanium-Alloy Ti-6Al-4V in Tensile and Compressive Loading Under Low, Medium and High Rates of Strain," in *Titanium Science and Technology*, G. Lutjering, U. Zwicker, and W. Bunk, eds., Deutsche Gesellschaft für Metallkunde.
13. Follansbee, P. S., and I. G.T. Gray (1989), "An Analysis of the Low Temperature, Low and High Strain-Rate Deformation of Ti-6Al-4V," *Metallurgical Transactions A*, **20A**, pp. 863–874.
14. Frost, H. J., and M. F. Ashby (1971), "Motion of a Dislocation Acted on by a Viscous Drag Through an Array of Discrete Obstacles," *Journal of Applied Physics*, **42**, No. 13, pp. 5273–5279.
15. Frost, H. J., and M. F. Ashby (1982), *Deformation Mechanism Maps*, Pergamon Press, Oxford.

16. Granato, A. V. (1973), "Microscopic Mechanisms of Dislocation Drag," *Metallurgical Effects at High Strain Rates*, Plenum Press, New York, New York, pp. 255–275.
17. Kumar, A., F. E. Hauser, and J. E. Dorn (1968), "Viscous Drag on Dislocations in Aluminum at High Strain Rates," *Acta Metallurgica*, **16**, pp. 1189–1197.
18. McClintock, F. A. (1968), "A Criterion for Ductile Fracture by the Growth of Holes," *Journal of Applied Mechanics*, **35**, pp. 363–371.
19. Rice, J. R., and D. M. Tracy (1969), "On the Ductile Enlargement of Voids in Triaxial Stress Fields," *Journal of the Mechanics and Physics of Solids*, **17**, pp. 201–217.
20. Kahlow, K. J., and B. Avitzur (1969), "Void Behavior as Influenced by Deformation and Pressure," American Iron and Steel Institute, Lehigh University. 

Uniform Etching of 85-Cm-Diameter Grating

Steven R. Bryan, Jr. and David L. Sanders

Manufacturing Materials Engineering Division

Mechanical Engineering

The purpose of this project was to extend the capability of an existing gridded, broad-beam (Kaufman-style) ion beam system to permit the uniform etching of a fused silica optic 85 cm in diameter with an etch depth uniformity within 5%. Since we hoped to demonstrate that we would be able to fabricate large size diffractive optics (for example, transmission gratings), a secondary requirement was to establish the etching conditions that allow such grating structures to have adequate efficiencies over this same large area.

We had hoped, during the course of this project, to fabricate a full size 85-cm diameter part. Since the substrate blanks for such gratings cost \$50,000 each and most of that cost would be sacrificed during an unsuccessful etch, we considered it important to demonstrate a reproducible and predictable process prior to risking such a blank. At this time, we believe we have demonstrated that we can etch such a part with minimal risk of failure. This was accomplished by etching a series of small gratings and fused silica etch witnesses mounted across this diameter, the data from which are presented in this report.

Introduction

During a joint effort between laser and engineering personnel at Lawrence Livermore National Laboratory (LLNL), an ion beam etching system having a 40-cm diameter gridded, broad-beam ion source was established. At the beginning of this project, this system was capable of etching a 30-cm part with an etch depth uniformity of better than $\pm 5\%$. Our goal was to extend our etching technology base to allow us to etch larger parts in the same system, with the ultimate goal of producing 85-cm-diameter transmission gratings with high efficiency across this full diameter. To accomplish this, we needed to develop a shadow mask allowing us to exactly cancel the inherent non-uniformity in the ion beam. We also needed to determine the etching parameters that are most critical for generating the desired grating profiles to minimize the risk of an unsuccessful etch on a large part.

Progress

Ion Source Modification

To make possible the uniform etching of such large parts, we needed to modify the existing ion

source to broaden the ion beam beyond the range for which it was designed. We first removed the original equipment internal baffle to permit use of the entire ion beam. We next removed the acceleration grids and re-installed them in a convex configuration to provide a de-focussed beam with a larger effective diameter. The result of these two modifications can be seen in **Fig. 1**. While the beam intensity is diminished, its diameter is increased. We needed this additional beam diameter to make it possible to etch our large part uniformly.

Substrate Holder and Etching Geometry

In addition to the ion source modifications, the substrate stage was modified to accept a single 85-cm-diameter substrate in place of the existing four 30-cm substrates. This was done while maintaining the ability to control substrate temperature.

Etch geometry, pictured in **Fig. 2**, was dictated by existing hardware: ion source and substrate stage horizontally opposed, with centers offset by 22 cm. The large disk which holds the 85-cm substrate is rotated with the ion source mounted off-center so that the entire surface is exposed to the ion beam during some portion its rotation about its center axis.

Model to Define Shadow Mask

To improve etch uniformity, a beam-shaping baffle was placed between the ion source and the substrate, as near to the substrate as possible. The determination of the shape of this baffle, which ultimately determines the etch uniformity, was critical to meet the goals of this project.

Dependable representation of the actual etch uniformity by a model is dependent upon consistent, reproducible operation of the ion source. Concerns about ion source repeatability were alleviated by periodically mapping the ion current density along a radius of the ion beam. As seen in **Fig. 3**, the current density profile of the ion source was found to correlate quite well to fused silica removal (etch) rates made at the same distances from the source. Ion source parameters, such as beam voltage, beam current, accelerator voltage, discharge voltage, and flow rates for various reactive gases were defined previously and held constant throughout this project.

The etch model was established by:

1. establishing the relationship between etch rate and position relative to the ion source;

2. identifying a second equation that describes the motion of any point on the substrate (relative to the ion source) as a function of time; and
3. substituting the position equation into the etch rate equation to yield etch rate as a function of time for any given point on the substrate.

By performing a numerical integration of etch rate over the period of time that the point on the substrate is in the ion beam, one can compute the etch depth at that point.

Initially, etch rates were measured by positioning fused silica samples in the ion beam, etching the sample for a period of time, then computing the etch rate by dividing the measured etch depth on the sample by the etch time. After the relationship between etch rates and beam current density measurements was established, a more economical method became available: ion current density measurements could be used to accurately predict etch rates. When confined to a plane that contains the surface of the substrate (27.5 cm from the ion source) and the perimeter of the ion beam, the radially symmetric beam yielded a fused silica etch rate that was found to conform well to the polynomial relation:

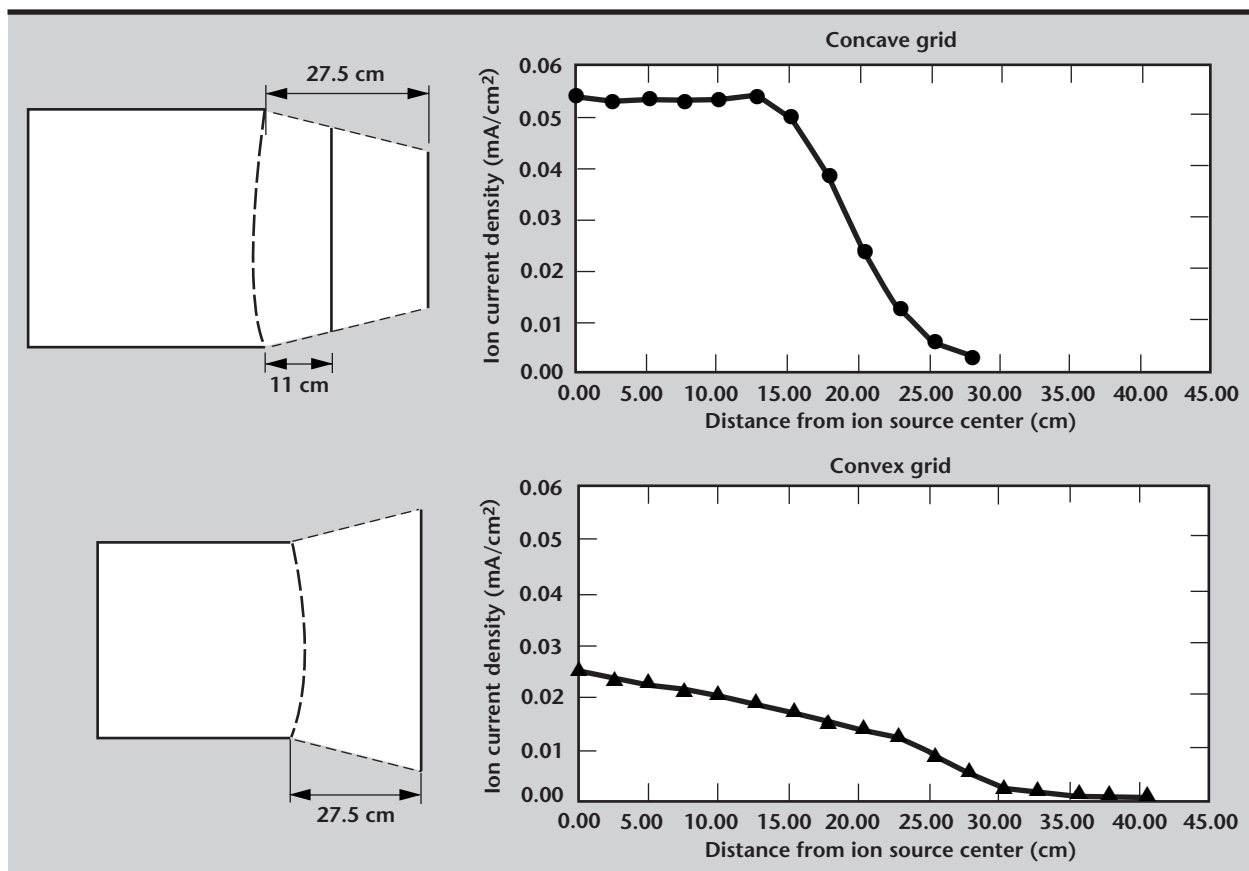


Figure 1. Effect on ion source beam diameter resulting from the source modification described in the text.

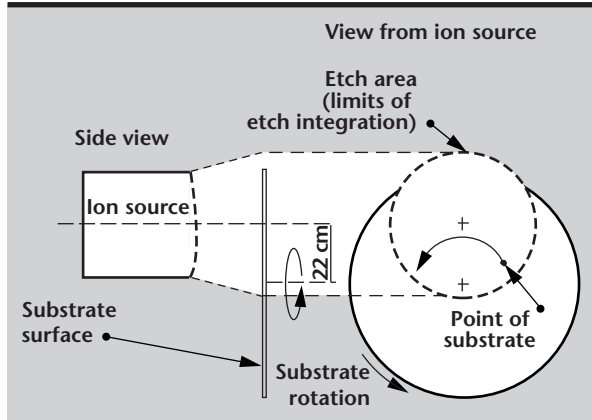


Figure 2. Etch geometry. The geometry was defined by existing hardware with the ion source and substrate horizontally opposed and the axes offset by 22 cm. The source-to-substrate distance was set to 27.5 cm.

$$E(r) = 1.42 - 4.41 \cdot 10^{-4} r + 3.06 \cdot 10^{-3} r^2 - 1.79 \cdot 10^{-4} r^3 + 2.72 \cdot 10^{-6} r^4, \quad (1)$$

where $E(r)$ is etch rate ($\mu\text{m/h}$) as a function of radial distance, r (cm), from the center of the ion source. From this equation, one can immediately

see that the etch rate in the center of the ion source, at a distance of 27.5 cm is $1.42 \mu\text{m/h}$ (Eq. 1 and Fig. 3).

The distance between a point on the substrate and the ion source center at any given time is dependent upon two variables: the location of the point on the substrate and the angle of substrate rotation at the time the distance is measured. Applying the Pythagorean theorem to the etch geometry in Fig. 4 yields the simple relation: $r^2 = x^2 + y^2$ (where r is distance from the center of the ion source). Substituting for variables x and y , the equivalent in terms of substrate rotation angle, θ , and distance between substrate center and the point of interest, r_s (Fig. 4), yields:

$$r^2 = (22 - r_s \cos \theta)^2 + (r_s \sin \theta)^2.$$

Since the rotational angle is a linear function of time (t), one may substitute time for angle (θ), simplify the equation, and solve for only the positive root to produce a usable function:

$$r(r_s, t) = \sqrt{484 - 44r_s \cos(t) + r_s^2}. \quad (2)$$

Note that points on the substrate have been defined only by their distance from the center of the substrate. This is acceptable because all points on a

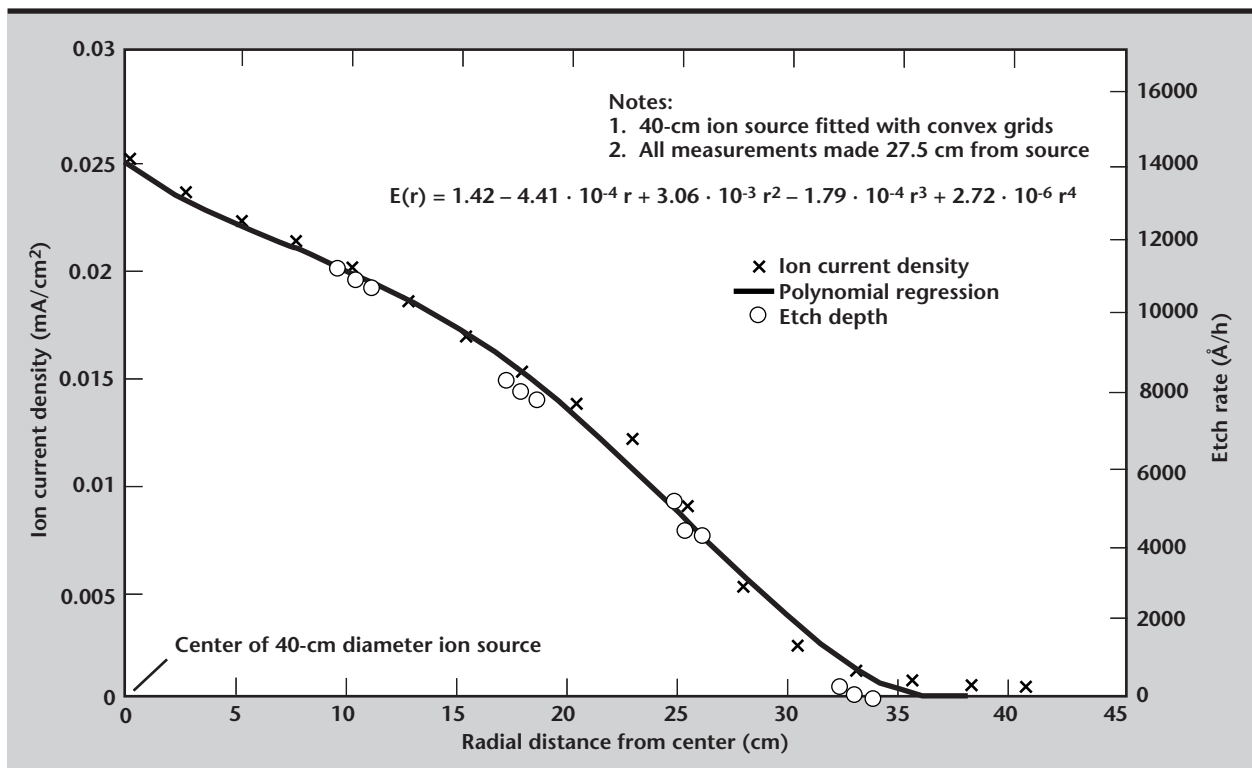


Figure 3. Ion beam profile comparison. Satisfactory correlation between Faraday cup measurements and fused silica etch rates were observed.

given circle of radius, r_s , on the substrate will be exposed to the same ion flux profile from the ion source, and will etch the same amount.

Substituting the equation defining radial distance from the source (Eq. 2) into the equation of etch rate (Eq. 1) above yields etch rate as a function of time for any point on the substrate. Integration of this etch rate over a period of time will provide a very close approximation of the total etch depth:

$$D(r_s, \theta_{\text{limit}}) = \int_0^{\theta_{\text{limit}}} E \times \left(\sqrt{484 - 44r_s \cos(t) + r_s^2} \right) dt, \quad (3)$$

where r_s is the location of any point on the substrate and θ_{limit} is a new variable; the upper limit of integration. This upper limit of integration, defined by the shape of a shadow-mask placed directly in front of the substrate (refer to Fig. 5), controls etch uniformity over the surface of the substrate. Increasing the value of θ_{limit} increases the amount of etch time on a revolution of the substrate, thus increasing etch depth on a particular circle of points on the substrate. Similarly, reducing the value of θ_{limit} will reduce etch depth for the same circle of points. As one can imagine, solving the resulting equation is tedious if not particularly complex, but is well suited to numerical integration by computer.

Figure 6 shows the effect of the shadow mask on the uniformity of the etching. In the case without the mask, the etching rate varies by almost a factor of 7 over the part. With a properly designed mask this

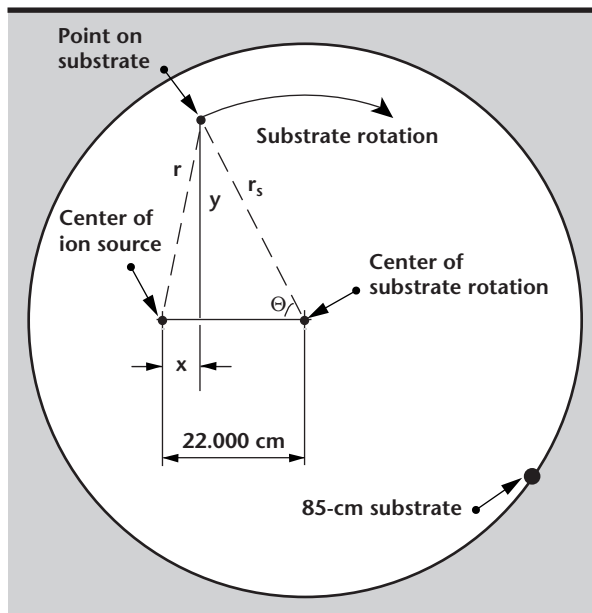


Figure 4. Location of point on substrate. Note that all points can be defined in terms of radial position on substrate. θ is a linear function of time.

variation is seen to be within the goal of $\pm 5\%$ over most of the part. (There remains a small area less than 2 cm at the center of the part that is slightly out of tolerance, but we are confident that this can be corrected with a minor adjustment of the position of the mask if such an adjustment is deemed necessary).

Grating Structures

As mentioned in the introduction, in addition to the necessary uniformity in etching rate, it will be necessary to etch steep walled grating structures to achieve the required diffraction efficiency. Figure 7 shows a scanning electron microscope photograph of a fracture surface of such a grating structure. Similar profiles were observed across the entire width of the grating, indicating that the desired etching behavior can be obtained with our current etching parameters.

Other Important Process Parameters

Initially, based on the experience of others, we assumed that it would be necessary to cool the part being etched to avoid overheating the photoresist. (Such overheating can make the photoresist difficult to remove after the completion of the etching process). To accomplish this cooling, we designed the substrate holder around a thermally conductive dry-chuck material normally used for cooling substrates during ion-etching operations in the semiconductor industry. For our particular application, however, we

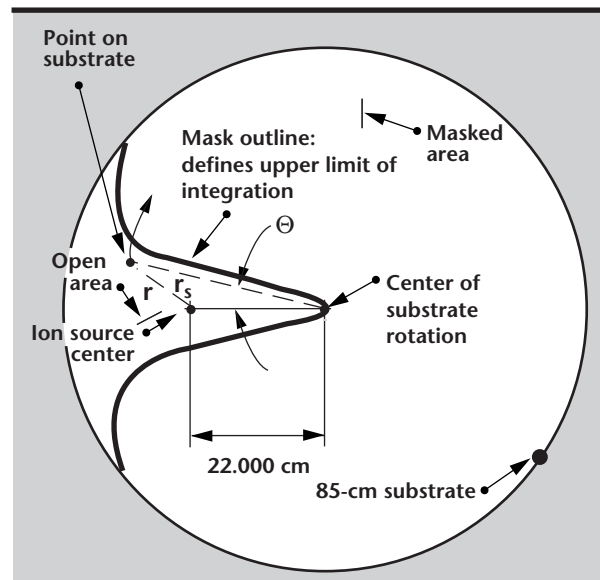


Figure 5. Approximate position and shape of limit-defining shadow mask.

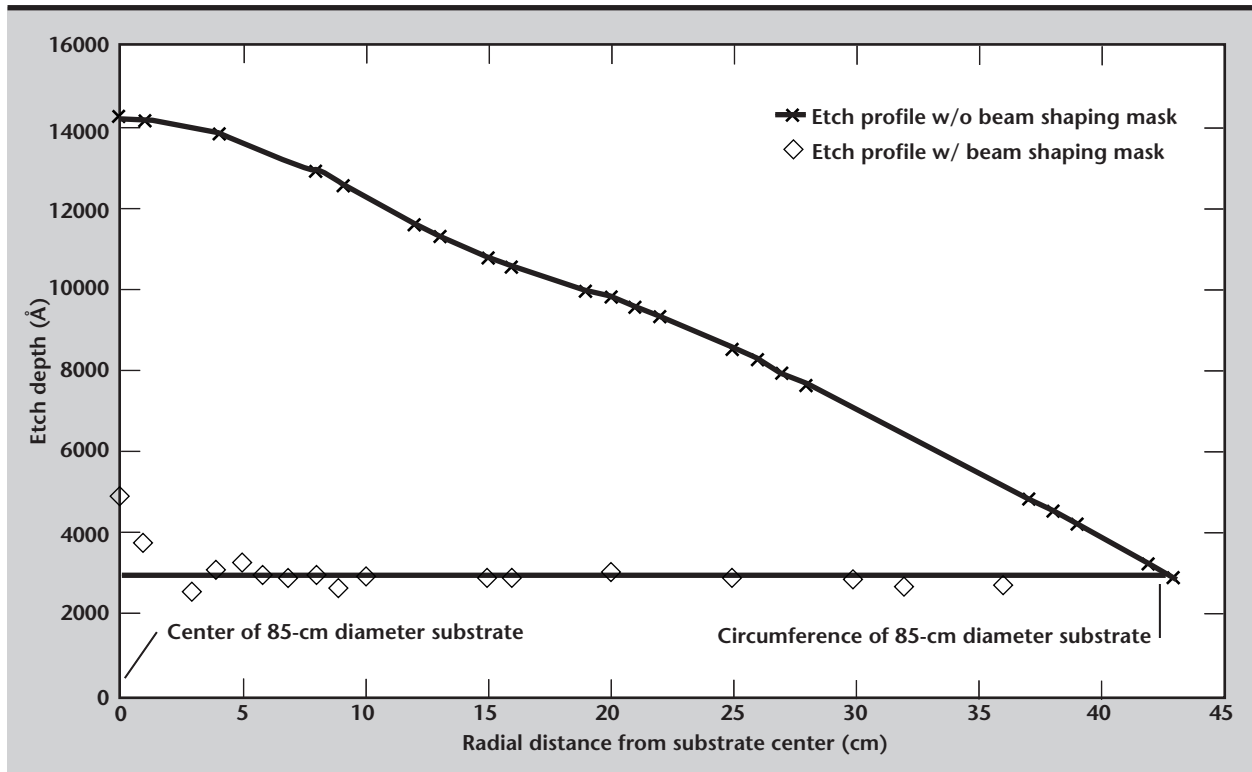


Figure 6. Effect of the shadow mask pictured in Figure 5 on the etch uniformity across an 85-cm-diameter part. Since the part is rotated, this figure represents half of the full diameter.

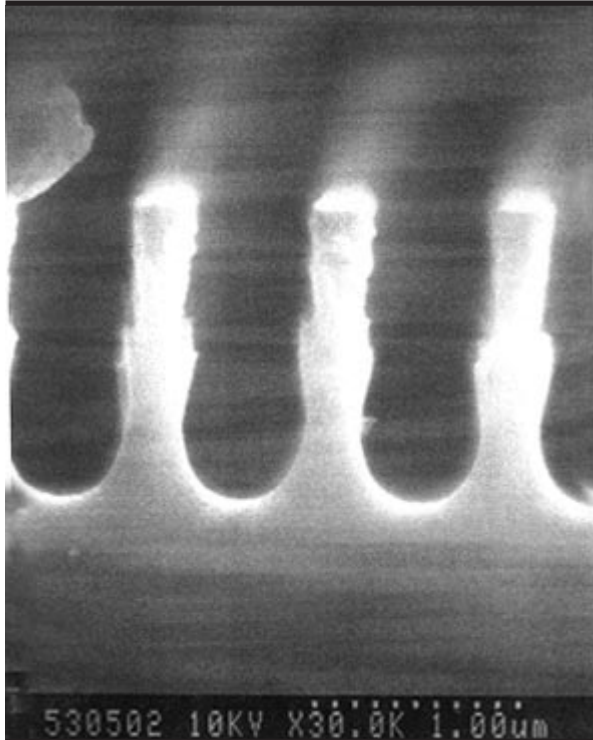



Figure 7. SEM micrograph of a grating structure etched using the current system.

discovered that cooling to temperatures below room temperature was not desirable because it contributed to the build-up of a hydrocarbon deposit in the trenches of the grating. In fact, we found it necessary to allow the substrate to be heated by the ion beam to prevent such buildup. In the future, we will need to investigate this temperature effect in more detail to determine the optimal etch temperature.

A second somewhat unexpected effect was the effect of buildup of a slightly conductive film on the ion gun insulators during the etching process. This buildup was found to lead to a reduction of the ion (etching) current during the etching run by as much as 20%. Recognizing this effect allowed us to compensate by adjusting the ion source to maintain a constant ion etching current throughout the course of the run.

Future Work

As funding and time permit, we plan to etch an 85-cm fused silica grating optic using the parameters we have established during this project. Based on our measurements, we expect the resulting grating will have the required etch depth uniformity and grating profile over the full diameter. 

istributed Sensor Inertial Measurement Unit

Carlos A. Avalle

*Defense Sciences Engineering Division
Electronics Engineering*

John I. Castor

Defense and Nuclear Technologies

We have developed a new type of Inertial Measurement Unit (IMU) in support of flight tests, based on a set of linear accelerometers distributed inside the flight vehicle. This novel, gyroscope-free design overcomes the restriction for sensors at or near the body's center of gravity (CG). The IMU is capable of determining the kinematics of a rigid body with six degrees of freedom. We have developed the mathematical model and are currently building the hardware for tests.

Introduction

Spacecraft motions are typically measured by IMUs capable of six degrees of freedom (that is, linear and angular motions about three orthogonal axes). Typically, these units consist of integral packages or sensors which are located at, or in the vicinity of, the CG. Our project addresses the need to keep the vicinity of the CG free from IMU equipment, and to avoid the excessive weight of gyroscopes. Thus, we have developed an IMU system that uses only accelerometers, none of which are at the CG.

The theory of accelerometer-only IMU systems is based on the relation

$$\mathbf{a} = \mathbf{n} \cdot A_{cm} + \mathbf{n} \cdot \dot{\boldsymbol{\omega}} \times \mathbf{R} + \mathbf{n} \cdot \boldsymbol{\omega} \times \boldsymbol{\omega} \times \mathbf{R} \quad (1)$$

where \mathbf{a} is the accelerometer response; A_{cm} is the acceleration of the CG; \mathbf{R} is the accelerometer location relative to the CG; \mathbf{n} is its sensing direction; $\boldsymbol{\omega}$ is the angular velocity vector of the body; and $\dot{\boldsymbol{\omega}}$ is the angular acceleration vector.

All the vectors are in the rotating frame of the body. For conventional IMUs, three gyroscopes are used to give the three components of $\boldsymbol{\omega}$ directly. Then three accelerometers, with mutually perpendicular sensing directions, give the information needed to find A_{cm} , since the angular acceleration and centripetal acceleration terms in the equation for \mathbf{a} (the second and third terms) can be estimated from the gyroscopic data and subtracted.

The rest of the navigation problem, as discussed by Regan and Anandakrishnan,¹ is to integrate the angular rates over time and find the true orientation of the body in space at each instant. The body-frame acceleration can then be transformed to the inertial-frame acceleration, which is then itself integrated to give the true velocity and location of the body.

It is possible to determine the complete motion of a body from acceleration measurements only. Using nine or more accelerometers in different locations with different sensing directions, A_{cm} , $\boldsymbol{\omega}$ and $\dot{\boldsymbol{\omega}}$ can be determined simultaneously. Various methods have been proposed.² The number of accelerometers is reduced to six if $\boldsymbol{\omega}$ is found by integrating $\dot{\boldsymbol{\omega}}$. This procedure can be numerically unstable.²

Our design, based on the paper by Chen, Lee and De Bra,³ chooses a special set of locations and orientations for six accelerometers, for which $\dot{\boldsymbol{\omega}}$ is obtained independently of the current value of $\boldsymbol{\omega}$, avoiding numerical instability. In this design, the six accelerometers are placed at the centers of the six faces of a cube, with the center of the cube at the CG (**Fig. 1**). The sensing axis of each accelerometer is along one of the diagonals of the cube face on which it lies, with opposing sensors using diagonals that are crossed. (The diagonals will form a regular tetrahedron.)

We have found that a much more general geometry is possible, with most of the advantages of the one in Reference 3. We found that the cube can be replaced by an arbitrary parallelepiped. That means

that the six sensor locations can be any six points that form a figure—a general octahedron—with a center of symmetry. The center of symmetry does not have to be the CG. The six sensors would be placed at the six vertices of the octahedron. The sensing directions are parallel to the diagonals of the parallelogram faces on which the sensors lie. Diametrically opposed sensors choose alternate diagonals of their respective parallel faces.

The only simplicity of the cubical layout of Reference 3 that is not preserved is the ease of solving the six equations for the components of $\dot{\omega}$ and the components of A_{cm} . With the more general arrangement a non-trivial system of six linear equations in six unknowns must be solved at each time. Since the matrix does not vary, most of the work can be done in advance.

The system of linear equations to be solved is the following:

$$\begin{bmatrix} S & T \end{bmatrix} \begin{bmatrix} \dot{\omega} \\ A_{cm} \end{bmatrix} = \begin{bmatrix} a_i - n_i \cdot \omega \times \omega \times R_i \end{bmatrix}, \quad (2)$$

where the right-hand side is a column vector formed by letting the index i run from 1 to 6, that is, over the six sensors, and S and T are 6x3 matrices defined by

$$\begin{aligned} S &= [R_i \times n_i], \\ T &= [n_i] \end{aligned} \quad (3)$$

The solution may be written

$$\begin{aligned} \dot{\omega} &= M[a_i], \\ A_{cm} &= N[a_i - n_i \cdot \omega \times \omega \times R_i] \end{aligned} \quad (4)$$

in terms of matrices M and N obtained by inverting $[S \ T]$. The special geometry is responsible for the

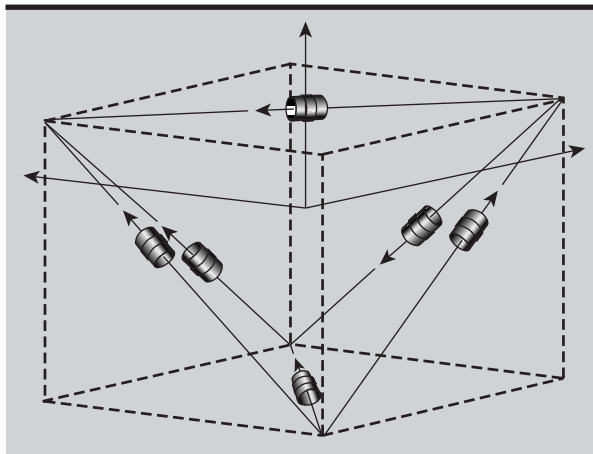


Figure 1. Six-accelerometer IMU configuration.

centripetal acceleration term not entering the result for $\dot{\omega}$. After $\dot{\omega}$ is obtained from the first equation, it is integrated forward in time to give the current ω , which is used in the second equation to find the acceleration of the CG. The other aspects of the navigation problem are carried out exactly as described above for the case of gyroscopes.

Progress

To evaluate the performance of the six-accelerometer design, we initially developed a computer model of the system. In the model, the test object is defined in terms of its mass and inertia. Input linear and angular forces on the test object can be defined at multiple locations, and these forces can be time varying. To evaluate the performance of the system, the model takes into account sensor locations and orientations, sensitivity, accuracy, integration times, and sampling periods. The model predicts velocities and acceleration time histories relative to inertial space, at any number of body-fixed points, in any body-fixed direction.

Currently, we are completing hardware development and fabrication for a test flight. Our system is based on Allied Signal QA-3100 inertial-grade accelerometers. These ultra-sensitive sensors are capable of resolution down to $<1 \times 10^{-7}$ g, with frequency response $DC < f < 1$ kHz.

Special signal conditioning was developed for our application. The accelerometer and signal conditioning hardware are shown in **Figs. 2** and **3**, in a photo, and a block diagram, respectively. One application required dynamic scale ranging to prevent high-frequency vibration and shock signals due to launch and flight vibration from saturating

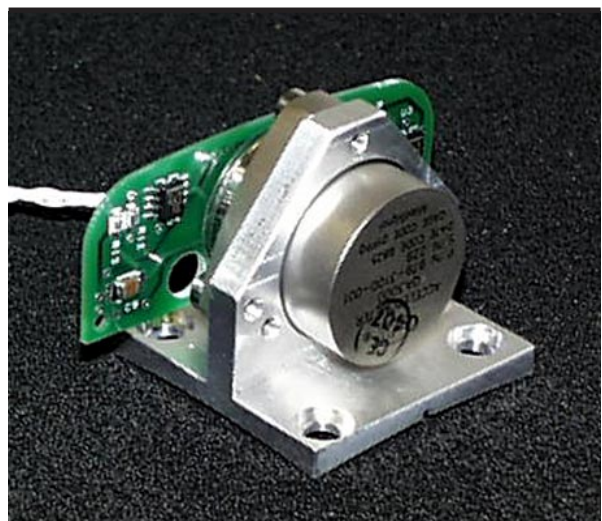


Figure 2. Photo of the accelerometer and signal conditioning hardware.

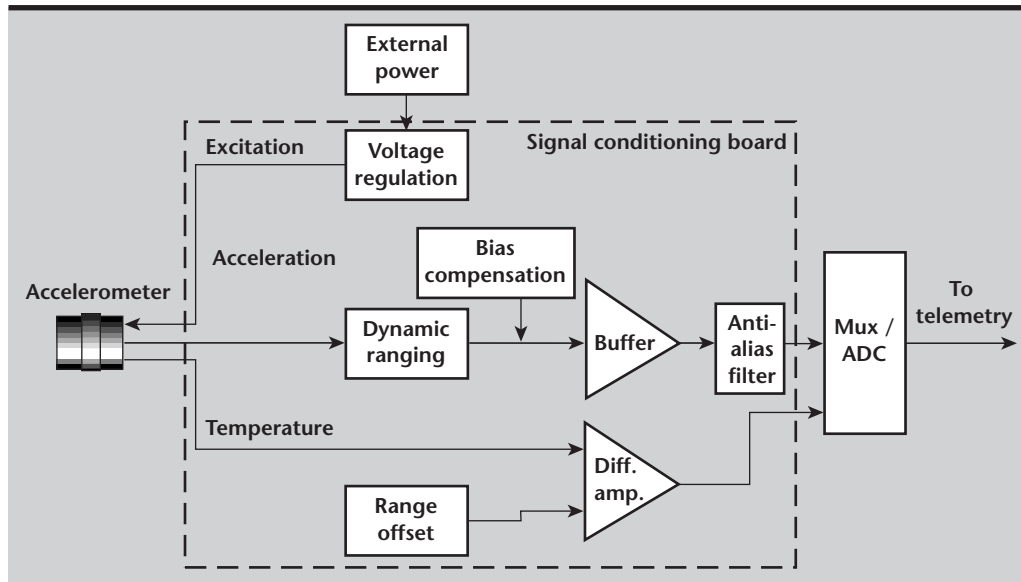


Figure 3. Block diagram of the accelerometer and signal conditioning electronics.

the sensor's output. These shock levels were unknown, thus requiring laboratory and field experiments to characterize and verify the response of sensors in these environments.

Initial attempts were made to isolate the sensors mechanically. However, ultimately that approach was supplanted by the electronic technique. These are true DC servo accelerometers, and as such, they exhibit a small output bias that is nulled prior to buffering and low-pass filtering. The accelerometers are also equipped with internal temperature sensors. Acceleration and temperature signals are digitized simultaneously, and a fourth-order temperature model is applied off-board for correction.


As presently configured for our flight test, the unit is set for a full scale range of ± 0.5 g. A standard 12-bit A/D converter provides a resolution of $< \pm 0.000250$ g, which translates to differential velocities on the order of 0.1 in./s and angular rates down to 0.25°/s for a duration on the order of 1 s.

In our flight test, acceleration and temperature data will be telemetered to ground stations and signals processed off-board. Control or closed-loop navigation applications could be realizable by on-board signal processing, the algorithms based on equations presented earlier.

Future Work

In the period of one year we have completed the development and are currently building the hardware for flight tests. The system has been optimized to work in a zero-g environment, which would be difficult to test in the laboratory. We are taking advantage of an opportunity to test the unit in an upcoming flight test and are presently completing integration of the system into the flight vehicle. Results of the test will not be known for several months, at which time a determination will be made regarding further development.

References

1. Regan, F. J., and S. M. Anandkrishnan (1993), *Dynamics of Atmospheric Re-Entry*, AIAA, Washington, D.C., Ch. 14.
2. Padgaonkar, A. J., K. W. Krieger, and A. I. King (1975), "Measurement of Angular Acceleration of a Rigid Body Using Linear Accelerometers," *ASME Journal of Applied Mechanics*, **42**, pp. 552-556.
3. Chen, J.-H., S.-C. Lee, and D. B. De Bra (1994), "Gyroscope Free Strapdown Inertial Measurement Unit by Six Linear Accelerometers," *Journal of Guidance and Control*, **17**, pp. 286-290. 

Fiber-Based Phase-Shifting Diffraction Interferometer for Measurement and Calibration of the Lick Adaptive Optics System

Eugene W. Campbell

*Advanced Microtechnology Program
Laser Programs*

Jong R. An

*Laser Engineering Division
Electronics Engineering*

An all-fiber based phase-shifting diffraction interferometer (PSDI) has been developed and integrated into the Lick Observatory adaptive optics system. Preliminary testing shows that the interferometer has a single measurement accuracy of 18 nm RMS, and can achieve better than 6 nm RMS with nine averages. The PSDI now needs to be incorporated into the control loop for the deformable mirror. The system then can be tested during an actual run on the Shane telescope. There are a few engineering difficulties to be overcome, but their solutions are straight forward.

Introduction

This project was initiated to integrate a PSDI into the adaptive optics (AO) system developed by Lawrence Livermore National Laboratory (LLNL) for use on the Shane telescope at Lick Observatory. Adding an interferometer to the AO system is useful for calibrating the control sensors, measuring the aberrations of the entire AO optical train, and measuring the influence functions of the individual actuators on the deformable mirror. A PSDI is particularly well suited for this application. A PSDI operates by using diffraction from a point-like aperture to generate a highly spherical wave that is compared interferometrically to an aberrated spherical wavefront.¹

Since the Lick AO system can be considered a black box that relays an aberrated point image to a corrected, diffraction-limited point image, the reference wave output by the PSDI can be fed without modification into the AO system. Likewise, the corrected output of the AO system can be fed without modification into the input of the PSDI. Thus, the only aberrations measured by the PSDI will be those of the AO system. This provides an extremely accurate measurement of the optical properties of the AO system.

Usually, the input to the AO system is the image created by the 3-m Shane telescope.² Because of atmospheric turbulence, this image is distorted and blurred. The AO system uses a fast moving tip-tilt mirror, which corrects for the blurring due to image movement, and a deformable mirror, which corrects for the image distortion.

The tip-tilt mirror is placed in the expanding beam, and the deformable mirror is placed in collimated light between two parabolic mirrors. The first parabola collimates the input point image, and the second parabola focuses the corrected planar wavefront to create a corrected point image. This image is then re-imaged by a scientific camera operating in the infrared.

There are also six auxiliary optics in the system: two are dichroic mirrors, used for splitting off light for the sensors that control the tip-tilt and deformable mirrors, and four are beam-steering mirrors (**Fig. 1**).

All totalled, the image created by the AO system passes through or reflects off of 11 optical elements. For this reason, it is not sufficient to simply replace the deformable mirror with a flat mirror and measure the aberrations right after the flat, as is currently done. This procedure accounts for all the aberrations up to the flat, but leaves out the aberrations introduced beyond it. Using the PSDI to measure the

system aberrations allows the wavefront sensor to be calibrated so that it corrects the image in a way that accounts for the aberrations of the entire optical train.

Progress

Design of the PSDI System

A difficulty in integrating a PSDI into the Lick AO system is that limited space is available for adding hardware. The PSDI systems developed at LLNL have a footprint of approximately 3 ft \times 3 ft. To make a system with a much smaller footprint, an entirely fiber optic system was developed. This system occupies a footprint of 9 in. \times 12 in., approximately 1/12 the size of the discrete systems. The vertical dimension also has been reduced, from 12 in. to 8 in. A CAD drawing of the system is shown in **Fig. 2**.

The all-fiber PSDI uses a 690-nm laser diode to provide 10 mW of optical power with a coherence length of approximately 3 m. This light is separated into two fibers by a variable beam-splitter that is set so that the beam intensities of each arm of the interferometer are equal. One fiber goes to the phase-shifter in the reference wave arm of the interferometer, and the other fiber goes to a fiber spool that is used to equalize the optical path lengths between the reference and test arms.

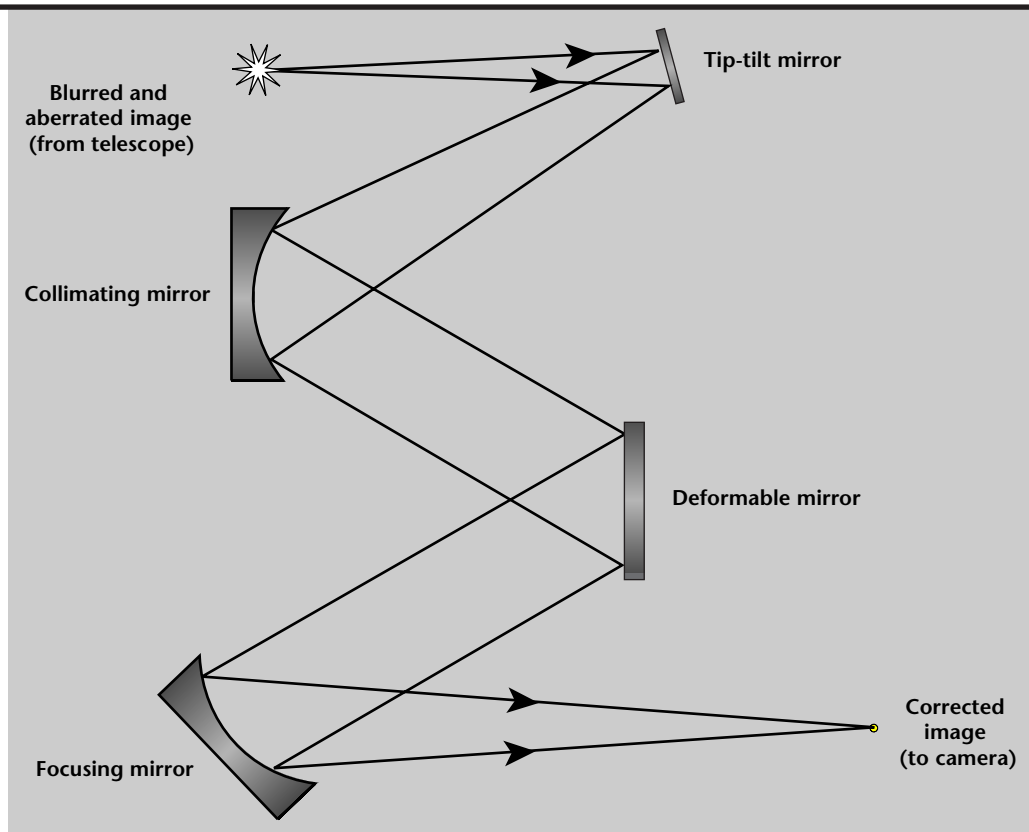
From there, the fibers go to polarization controllers (PLC) that are set so that the polarizations of the test and reference waves are identical at the camera. Upon leaving the PLCs, the fibers run to opposite ends of the AO system. The test fiber runs to the input point of the AO system, and the reference fiber runs to the output point of the AO system.

The phase-shifter is a commercially available device that consists of 25 windings of fiber around an oval spool. The spool has piezoelectric (PZT) plates along the two long sides. The fiber is epoxied to the PZT plates so that when a voltage is applied to the plates, the fiber is stretched as the plates grow in length. The fiber-based variable beam-splitter is also a commercial device, and is used to balance the beam powers at the CCD camera to achieve maximum fringe contrast.

Once the test wave passes through the AO system, it converges onto the end of the reference fiber. It then reflects off the reference fiber to combine with the diverging reference wavefront diffracting out of the end of the fiber. The end face of the reference optical fiber is super-polished (RMS roughness $< 1 \text{ \AA}$) to ensure that the reflected light is not distorted by the shape of the fiber end face.

These two beams are then steered by a knife-edge mirror through an imaging lens and onto a CCD camera. The knife-edge mirror passes half of the cone

Figure 1. Simplified representation of the Lick Observatory AO system.



of light diffracting from the reference fiber, and reflects half towards the camera. Since the numerical aperture of the beam exiting the AO system is very small ($f^\# \approx 27$), it is not clipped by the knife-edge as it focuses onto the reference fiber. This optical system that allows for the interference of the beams' test and reference waves is shown in **Fig. 3**.

Accuracy of the Initial System Test

The PSDI was mounted on the AO system bread-board and initial repeatability tests were performed. It was expected that air currents in the 5.8-m optical path and vibrations of the eight reflective optics would lead to noise in the measurement. However, since

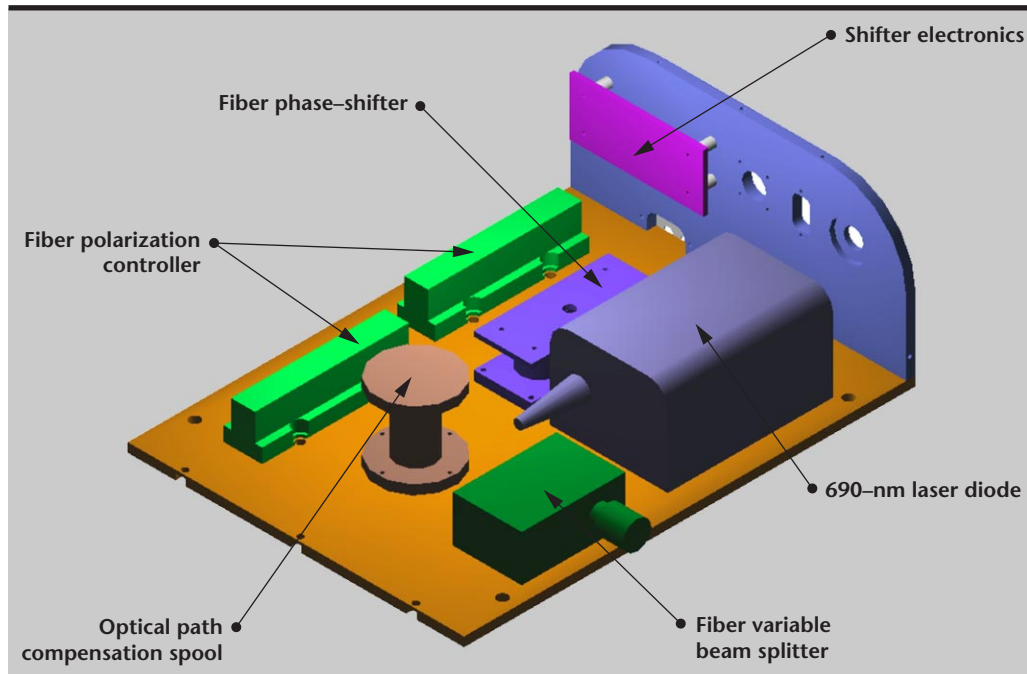


Figure 2. Front-end design of the PSDI system.

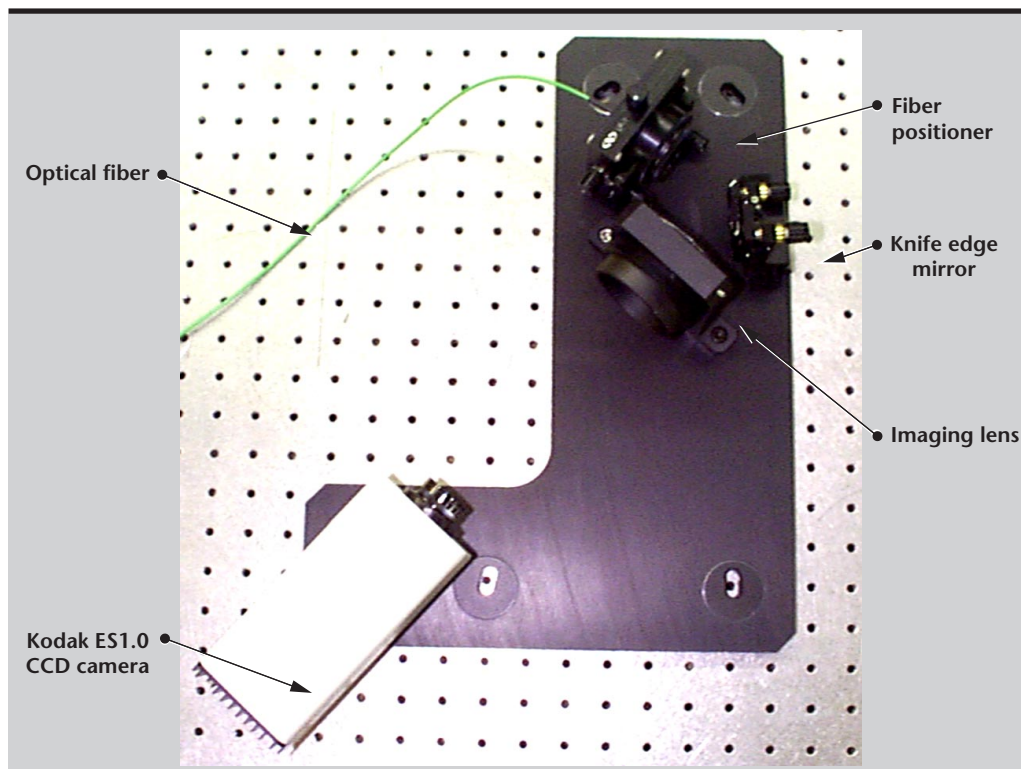


Figure 3. Optical system. The reference wavefront diffracting from optical fiber combines with test wavefront from the AO system and interferes at the camera.

Table 1. Data from repeatability tests.

Number of averages	Average RMS error (nm)	Standard deviation
1	18.6	9.08
4	9.66	3.91
9	5.23	—
16	3.58	—

such noise is typically random, it is possible to make multiple measurements and average them to reduce the noise. Unfortunately, feedback into the laser caused instabilities in the source coherence, and it was necessary to take measurements one at a time. Each measurement was analyzed on the spot, and approximately one quarter of the measurements were rejected due to laser instability. A total of 25 measurements were kept. In the future, a Faraday-type optical isolator will be used to prevent laser feedback.

The complete set of 25 measurements was averaged together to form a baseline measurement. Then each measurement was individually compared to the baseline. The typical difference between a single measurement and the baseline was 18.6 nm RMS, with a standard deviation of 9.1 nm RMS. Averaging groups of four measurements, and comparing them to the baseline yielded an error of 9.7 nm RMS, with a standard deviation of 3.9 nm RMS.

As expected for N measurements of a system with random noise, the RMS error dropped as $1/\sqrt{N}$. As groups of nine and 16 were compared to the total set,

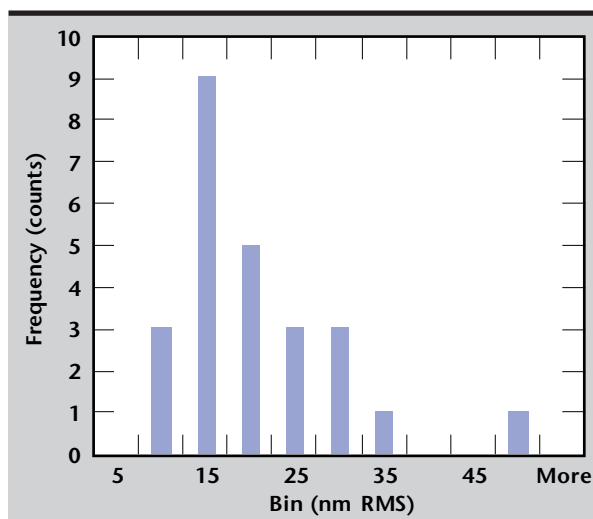


Figure 4. Histogram of the single measurement errors.

the noise dropped more quickly. This is because these groupings no longer appear like independent measurements when compared to a baseline formed with only 25 measurements. The various groupings are given in Table 1.

A histogram for the single measurement results is shown in Fig. 4, where each bin is 5 nm wide. The minimum difference was 7.8 nm RMS, and the maximum was 48 nm RMS. As can be seen, it is reasonable to treat the noise as random, and nine or more averages should yield a measurement with an RMS error of less than 10 nm. To achieve an accuracy of better than 1/100 of a wave in the visible region, approximately 16 averages would be required. At a processing time of 8 s/average, it will take approximately 2 min to make a measurement accurate to better than 1/100 of a wave.

Wavefront Measurement at the Deformable Mirror

In all the measurements, the imaging lens was focused on the deformable mirror, which forms the pupil of the AO system. Therefore, the optimal deformations of the mirror needed to improve the wavefront can be calculated if the influence functions of the individual actuators are known.

A measurement of the wavefront at the deformable mirror is shown in Fig. 5. The peak-to-valley deviation of this wavefront is $1.65\text{ }\mu\text{m}$, and the RMS deviation is 133 nm. This wavefront is flat to within 1/6 of the 632.8 nm measurement wavelength, which corresponds to a Strehl ratio of 0.36. The accuracy of this measurement is approximately 4 nm RMS. When the

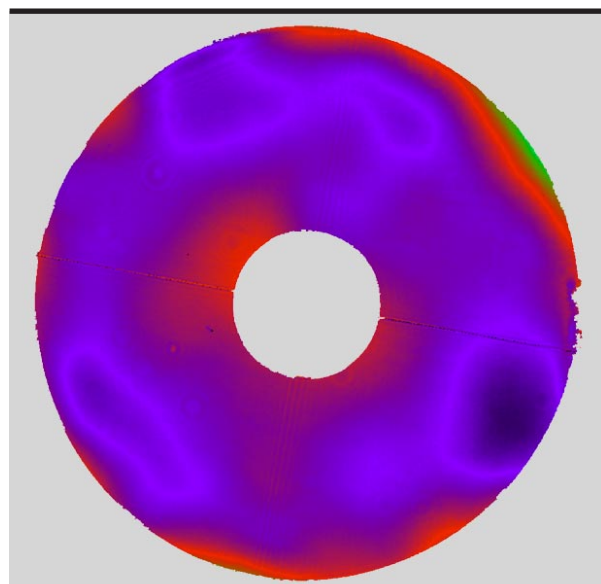


Figure 5. Wavefront of the AO system imaged at the deformable mirror.

wavefront has been freshly flattened using the phase diversity method, Strehl ratios of 0.45 have been obtained. Interactive manipulations of the actuators have yielded Strehl ratios as high as 0.6.

It is expected that the PSDI can be used to flatten the wavefront to obtain Strehl ratios better than 0.8. It should be noted that improving the Strehl ratio from 0.36 to 0.8 at $0.532\text{ }\mu\text{m}$, only improves the Strehl ratio at $2.2\text{ }\mu\text{m}$ from 0.92 to 0.98. The real advantage in using the PSDI to calibrate the system is that it takes much less time than the current method and is more reliable.

Influence Function of a Single Actuator

A measurement can also be made when a single actuator is either pushed or pulled. The baseline measurement can then be subtracted from this measurement, and the difference yields the influence function for the particular actuator. **Figure 6** shows

two measurements of the influence function of mirror actuator #14 as it is pushed and pulled. As can be seen in both measurements, the influence function of the actuator is roughly Gaussian in nature. However, there is a slight hexagonal shape to the deflection because of the hexagonal layout of the actuators. Lineouts through the centers of the deflections better display the magnitude of the wavefront change and are also shown in **Fig. 6**.

Note that this is not equal to the actual mirror deformation. The wavefront deformation is doubled relative to the mirror deformation because of the reflection, and there is also an obliquity factor due to the light not being normally incident. The “pull” data is for a D/A voltage of -4.569 V on the actuator, and the “push” data is for D/A voltage of 4.781 V . An image of the fringes in the pushing and pulling modes is shown in **Fig. 7**. Note that ~ 30 to 60 tilt fringes have been introduced to overcome problem of multiple pass noise.

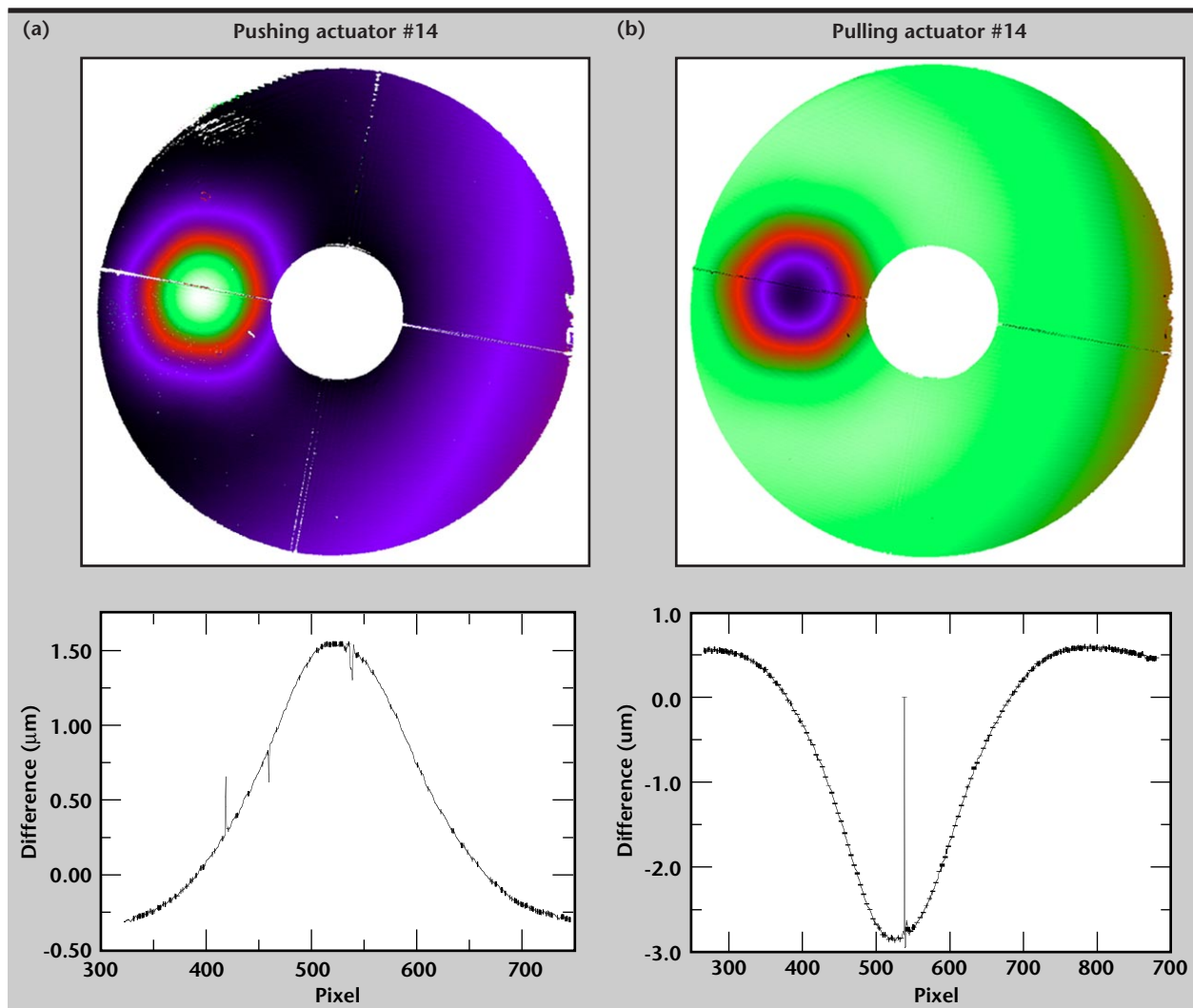


Figure 6. Measurements of influence function of mirror actuator as it is a) pushed and b) pulled.

Actuators at the center of the field and at the edge were also moved to verify the actuator location map. The images in **Fig. 8** show the wavefront difference from the baseline as actuators #02 and #31 were pulled.

During the first year of this experiment, we accomplished the following: 1) developed an all-fiber PSDI system of extremely small size; 2) qualified a fiber-optic phase-shifter to better than 1 nm accuracy; 3) wrote software to control the PSDI and acquire data from a PC running Windows NT; 4) integrated the PSDI system onto the AO bench in a way that least disturbed the existing layout; and 5) used the PSDI system to make preliminary measurements of the AO system.

Future Work

Development of the PSDI system brought to light several problems that remain to be solved:

1. Laser source instability is limiting the accuracy of the PSDI system.
2. Light from the reference fiber is passing through the system, reflecting off the end of the input fiber, passing back through the system, and creating spurious noise fringes.
3. Both dichroics in the AO system must be removed to use the PSDI because the dichroics do not pass sufficient energy at the PSDI laser source wavelength.

Figure 7. Image of fringes in the a) pushing and b) pulling modes.

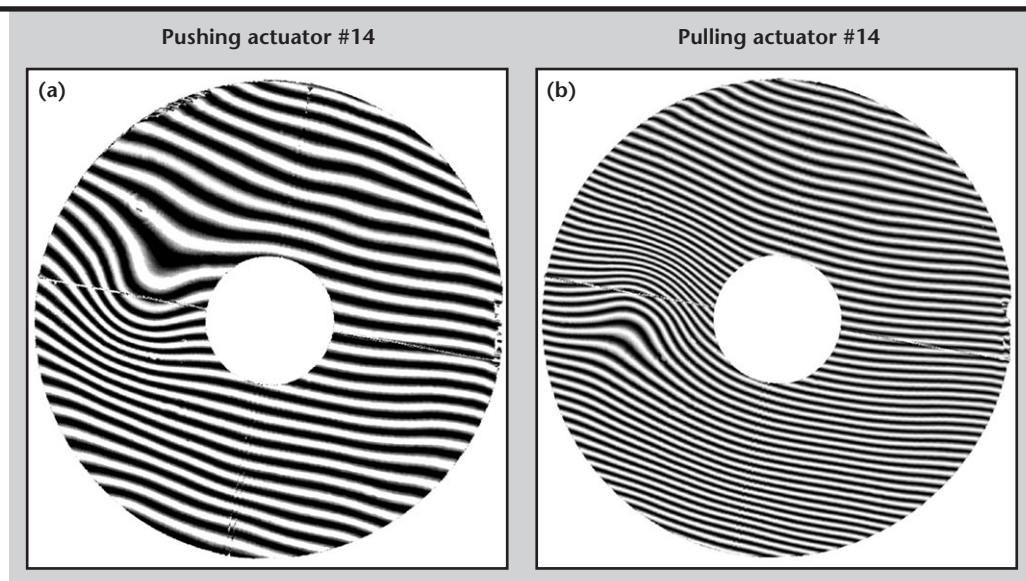
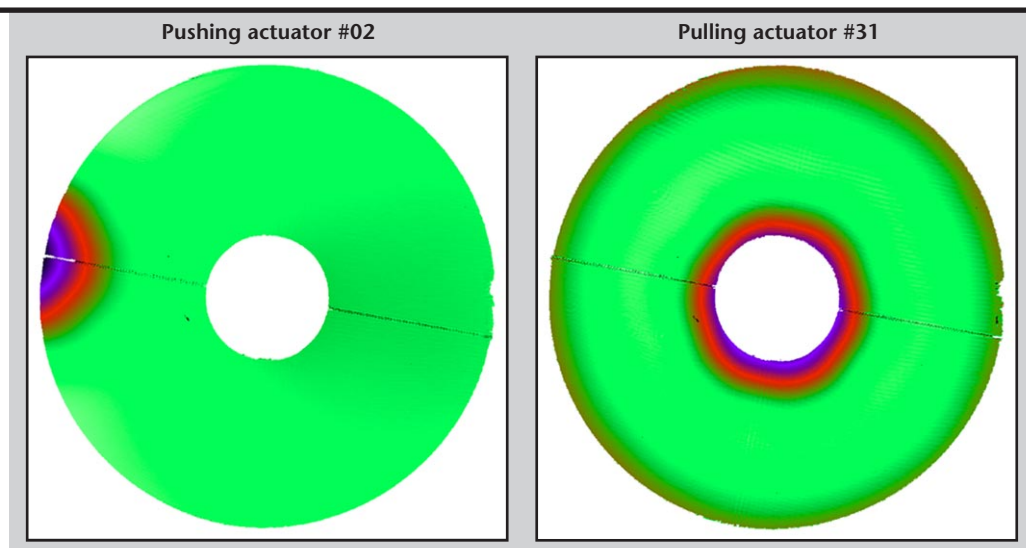


Figure 8. Images showing wavefront difference from baseline as actuators were pulled.



4. The PSDI system has yet to be used while the AO system is mounted on the Shane telescope.
5. Some of the more expensive equipment is on loan from the EUVL program and needs to be replaced.
6. If the system is to become a permanent feature at Lick Observatory, it will have to be converted to use a Sun workstation.

References

1. Sommargren, G. E. (1996), "Diffraction methods raise interferometer accuracy," *Laser Focus World*, pp. 61–71, August.
2. Olivier, S. S., and C. E. Max (1997), "First significant image improvement from a sodium-layer laser guide star adaptive optics system at Lick Observatory," Lawrence Livermore National Laboratory, Livermore, California (UCRL-JC-128088). 